Title: Cholangiocyte organoids can repair bile ducts after transplantation in human liver.

Authors: Fotios Sampaziotis[1,2,3,*], Daniele Muraro[1], Olivia C. Tysoe[1,4], Stephen Sawiak[5], Timothy E. Beach[4], Edmund M. Godfrey[6], Sara S. Upponi[6], Teresa Brevini[1], Brandon T. Wesley[1], Jose Garcia-Bernardo[7], Krishnaa Mahbubani[4], Giovanni Canu[1], Richard Gieseck III[8], Natalie L. Berntsen[9,10,11], Victoria L. Mulcahy[2,12], Keziah Crick[13], Corrina Fear[13], Sharayne Robinson[13], Lisa Swift[13], Laure Gambardella[1,2], Johannes Bargehr[1,2,14], Daniel Ortmann[1], Stephanie E. Brown[1], Anna Osnato[1], Michael P. Murphy[15], Gareth Corbett[16], William T. H. Gelson[2,3], George F. Mells[2,3,12], Peter Humphreys[1,] Susan E. Davies[17], Irum Amin[4,13], Paul Gibbs[4,13], Sanjay Sinha[1,2], Sarah A. Teichmann[7,18], Andrew J Butler[4,13], Teik Choon See[6], Espen Melum[9,10,11,19,20], Christopher J. E. Watson[4,13,21,22], Kourosh Saeb-Parsy[4,13, †], Ludovic Vallier[1,4†*]

Affiliations:

1. Wellcome and MRC Cambridge Stem Cell Institute.
2. Department of Medicine, University of Cambridge.
3. Cambridge Liver Unit, Cambridge University Hospitals NHS Foundation Trust.
4. Department of Surgery, University of Cambridge and NIHR Cambridge Biomedical Research centre, Cambridge, UK
5. University of Cambridge, Department of Clinical Neurosciences, University of Cambridge, Cambridge, UK.
6. Department of Radiology, Cambridge University Hospitals NHS Foundation Trust.
7. Wellcome Sanger Institute, Wellcome Genome Campus, Hinxton, Cambridge CB10 1SA, UK.
8. Immunopathogenesis Section, Laboratory of Parasitic Diseases, National Institute of Allergy and Infectious Diseases, NIH, Bethesda, MD 20852, USA

9. Norwegian PSC Research Center, Department of Transplantation Medicine, Division of Surgery, Inflammatory Diseases and Transplantation, Oslo University Hospital Rikshospitalet, Oslo, Norway.
10. Research Institute of Internal Medicine, Division of Surgery, Inflammatory Diseases and Transplantation, Oslo University Hospital, Oslo, Norway.
11. Institute of Clinical Medicine, Faculty of Medicine, University of Oslo, Oslo, Norway.
12. Academic Department of Medical Genetics, University of Cambridge, Cambridge, UK.
13. Department of Surgery, Cambridge University Hospitals NHS Foundation Trust, Cambridge, UK.
14. Division of Cardiovascular Medicine, University of Cambridge, ACCI Level 6, Box 110, Addenbrooke's Hospital, Hills Road, Cambridge CB2 0QQ, UK.
15. MRC Mitochondrial Biology Unit, University of Cambridge, Cambridge, UK.
16. Cambridge University Hospitals NHS Foundation Trust
17. Department of Histopathology, Cambridge University Hospitals NHS Foundation Trust, Cambridge, UK.
18. Cavendish Laboratory, JJ Thomson Ave, Cambridge CB3 0HE, UK.
19. Section for Gastroenterology, Department of Transplantation Medicine, Division of Surgery, Inflammatory Diseases and Transplantation, Oslo University Hospital Rikshospitalet, Oslo, Norway.
20. Hybrid Technology Hub-Centre of Excellence, Institute of Basic Medical Sciences, Faculty of Medicine, University of Oslo, Oslo, Norway.
21. National Institute of Health Research (NIHR) Cambridge Biomedical Research Centre, and the NIHR Blood and Transplant Research Unit (BTRU) at the
22. University of Cambridge in collaboration with Newcastle University and in partnership with NHS Blood and Transplant (NHSBT), Cambridge, UK

† These authors share senior authorship.

*Correspondence to: Fotios Sampaziotis, fs347@cam.ac.uk; Ludovic Vallier, lv225@cam.ac.uk.

One sentence summary:

Single-cell RNA sequencing analyses combined with a novel model for cell transplantation in human livers reveal that intra- and extra-hepatic cholangiocytes are interchangeable for regenerative medicine applications.

Abstract:

Organoid technology holds great promise for regenerative medicine but has not yet been applied to humans. Here, we address this challenge in the context of cholangiocyte organoids and cholangiopathies, which represent a leading indication for liver transplantation. Using single-cell RNA sequencing we show that primary human cholangiocytes display transcriptional diversity which is lost in organoid culture. However, cholangiocyte organoids remain plastic and resume their *in vivo* signatures when transplanted back in the biliary tree. We then utilize a new model of cell engraftment in human livers undergoing *ex vivo* normothermic perfusion to demonstrate that this property allows extrahepatic organoids to repair human intrahepatic ducts after transplantation. Our results provide proof-of-principle that cholangiocyte organoids can be used to repair human biliary epithelium.

Main text:

Organoids have a unique potential for tissue repair as they retain key functions and characteristics of their tissue of origin. Nevertheless, their ability to repair native epithelia and restore their complexity has not been established in humans, while organoid engraftment and survival *in vivo* has only been demonstrated in a limited number of animal studies (*1*). The bile duct epithelium presents an archetypal and clinically important system for addressing this challenge and for developing proof-of-concept studies in human. Indeed, disorders of the biliary system, which transfers bile from the liver to the duodenum, account for 70% of paediatric and up to a third of adult liver transplantation (*2*). This results in a pressing need for therapeutic alternatives, such as cell-based therapy. Furthermore, organoids suitable for regenerative medicine applications can be easily derived from biliary epithelial cells, known as cholangiocytes (*3*). Finally, the bile ducts also recapitulate the epithelial diversity found in other hollow-lumen organs (*4*). Indeed, different regions along the biliary tree display distinct transcriptional profiles and functional properties, such as the chemical modification of bile (*5*, *6*), as well as variation in disease susceptibility between the intrahepatic ducts, extrahepatic ducts and the gallbladder. Nevertheless, the impact of this regional variation on the characteristics and regenerative potential of the organoids derived from different regions of the biliary tree remains to be characterized. To address these questions and demonstrate the value of organoids for regenerative medicine in humans, we first characterize cholangiocyte diversity *in vivo* using single-cell transcriptomics and confirm that different regions of the human biliary tree contain cells with distinct transcriptional profiles. We then show that cholangiocytes lose these differences in organoid culture and become interchangeable, but their regional identity can be restored *in vitro* by environmental stimuli. We subsequently use a biliary injury mouse model and a novel model for cell transplantation in human organs undergoing *ex vivo* normothermic perfusion to prove that this plasticity allows cholangiocytes from one region to repair a different region of the biliary tree paving the way for cell-based therapy using organoids.

To characterize the cellular composition of the human biliary epithelium, cholangiocytes from different regions (Intrahepatic Bile Ducts (IHD): 5 patients, 7295 cells; Common Bile Duct (CBD): 3 patients, 3006 cells; Gallbladder (GB): 3 patients, 3702 cells) were isolated using magnetic bead sorting and their transcriptome was determined using droplet encapsulation single-cell RNA sequencing (scRNAseq) (**Fig. 1A-B, Fig. S1A-C**). The isolated cells expressed key cholangiocyte markers, including KRT7, KRT19, SOX9, and GGT **(Fig. S2A).** The transcriptomes of all three biliary cell populations shared a core transcriptional profile, illustrated by their proximity in UMAP space and high connectivity in Partition-based Graph Abstraction (PAGA) analysis when compared to different liver cell types, such as stellate cells and liver sinusoidal endothelial cells (LSECs, **Fig. S2B-S2E**). However, more detailed analysis after sub-clustering of cholangiocytes revealed non-overlapping expression modules of the three populations **(Fig. 1B)**. This suggests that, despite their similarities, cholangiocytes from different regions exhibit unique gene expression signatures (*6*). Accordingly, Differentially Expressed Genes (DEG) analysis **(Data S1)** identified known region-specific markers, including aquaporins (*7*), mucins (*8*), *FGF19* (*9*), *SOX17* (*10*) in the extrahepatic biliary tree, *JAG1* (*11*), *TACSTD2* (*12*) and YAP target genes in intrahepatic cholangiocytes (*13*, *14*), as well as novel markers including *DCDC2*, *TFF1-3, SLC15A1* **(Fig. 1C-1D, Fig. S3A-S3D)**. Most of these genes correspond to functional markers such as bile acid receptors or channels modifying bile composition **(Fig. S3C)**. Thus, the transcriptional divergence among cholangiocytes from different regions could reflect adaptation to their microenvironment, such as variation in bile properties along the biliary tree (*15*). Accordingly, cholangiocytes from anatomically adjacent and hence environmentally similar regions (e.g. intrahepatic and common bile duct vs. gallbladder) displayed higher transcriptional similarity. This was illustrated by PAGA analysis **(Fig. S3E-S3F)**, in agreement with results from diffusion pseudotime (DPT) and single-cell consensus clustering (SC3) analyses **(Fig. S4-S5).** These results point towards a progressive change in the expression of region-specific markers **(Fig. 1E, Data S2),** and a gradual transition in the transcriptional signature of cholangiocytes from adjacent regions **(Fig. S4A-S4C)** rather than distinct subpopulations **(Fig. 1E, S4-S5)**. This

gradient in gene expression is likely to support adjustment of the cells to environmental conditions, such as the gradual change in bile composition from the intrahepatic ducts to the gallbladder. In conclusion, our results show that the human biliary epithelium is comprised of cholangiocytes displaying a gradual shift in their transcriptional profile along the biliary tree, which is likely imposed by region-specific microenvironments.

We subsequently used this single-cell map of the human biliary tree as a framework to characterise cholangiocyte organoids. To this end, a fraction of the primary cholangiocytes isolated for scRNAseq from each region (IHD, CDB, GB) were propagated as organoids using our established conditions (*3*, *16*). The resulting organoids expressed cholangiocyte markers (KRT7, KRT19, SOX9, HNF1B, CFTR; **Fig. S6A-S6B**); displayed comparable functionality (ALP, GGT activity; **Fig. S6C-S6D**) and similar expansion potential regardless of their region of origin **(Fig. S6E)**. To further explore these similarities, we performed scRNAseq on these organoids (2 lines per region; GB: 5859 cells; CBD 5321 cells; IHD 6641 cells; **Fig. S1A-C**). UMAP and PCA analyses demonstrated that organoids exhibited overlapping transcriptomic profiles **(Fig. 2A, Fig. S7A-S7D)** indicating that cholangiocytes grown *in vitro* assume a similar transcriptional signature independent of their region of origin. Of note, regressing cell cycle-related genes did not change these observations excluding that a common "proliferation" signature could mask differences between organoids of different spatial origins **(Fig. S7A-S7C, S7E)**. Furthermore, we did not detect any cells co-expressing known somatic stem cell markers (*LGR5, PROM1, TACSTD2, NCAM*), excluding the possibility that organoid similarities reflect a common progenitor/stem cell identity **(Fig. S7F)**.

We then compared organoids from different regions with primary cholangiocytes to explore if these similarities corresponded to loss of their original regional identity *in vitro* **(Fig. 2A)**. Organoids and primary cells following cell cycle regression shared a core transcriptional profile reflecting their common cholangiocyte nature, which was illustrated by their proximity in UMAP space and high PAGA connectivity when compared to different liver cell types, such as stellate cells and LSECs **(Fig. S7C-D)**. However, DEG analyses highlighted downregulation of region-

specific markers, such as *SLC13A1* and *SLC26A3* **(Fig. 2B, Fig. S7G);** while Gene Ontology (GO) and Gene Set Enrichment Analyses (GSEA) identified these DEGs as factors facilitating the adaptation of cholangiocytes to their respective microenvironments, e.g. bile acid vs. culture medium processing genes **(Fig. S8A-S8C)**. Furthermore, we confirmed upregulation of YAP target genes (**Data S3**) in organoids, in accordance with previous reports (*14*). Consequently, primary cholangiocytes propagated as organoids adapt to their new microenvironment by maintaining their core transcriptional signature, while losing the expression of markers specific to their region of origin.

To explore the mechanisms controlling cholangiocyte identity, we decided to add bile in our culture conditions as the principal determinant of the cholangiocyte microenvironment. Different organoids (IHD, CBD, GB) were treated with human gallbladder bile for 72 hours and then characterized using scRNAseq **(Fig. 2A, S1A-S1C)** (GB: 3815 cells; CBD 3224 cells; IHD 3653 cells). UMAP and PCA revealed that treated organoids assumed a new overlapping gene expression profile **(Fig. 2A, S9A)** confirming a shared capacity to adapt to exposure to bile. Importantly, PAGA and DEG analyses showed that this transcriptional profile was shifted towards a gallbladder identity **(Fig. 2B, Fig. S9B-S9C)**. To characterise the factors controlling this transition, we interrogated differentially expressed genes in bile-treated organoids. GO, GSEA and UMAP analyses (**Fig. S9D-S9F)** confirmed the induction of region-specific markers (SOX17, MUC13, FGF19; **Fig. 2B, S9F**) and revealed upregulation of bile acid receptor pathways and downstream targets (*NR1H4/FXR, NR1I2, NR0B2, SLC51A, FGF19, ABCA1, PPARG*; **Fig. 2B, S9D-S9F**). Of note, these results were validated through activation and inhibition of the Farnesoid X receptor (FXR), using chenodeoxycholic acid and z-guggulsterone respectively **(Fig. 2C-2D)**, thereby confirming that regardless of their origin, cholangiocytes grown *in vitro* can respond and adapt to environmental stimuli. Together, these results suggest that cholangiocyte organoids could assume different regional identities when instructed by the appropriate niche factors.

To validate cholangiocyte plasticity and explore its functional implications, we decided to assess if organoids from one region of the biliary tree could repair a different region following transplantation. For this, we induced cholangiopathy in immunodeficient mice using 4,4'-methylenedianiline (MDA) (*17*) **(Fig. 3A-3B, S10, S11)** and attempted to rescue the phenotype with intraductal delivery (*18*) of human gallbladder organoids expressing Red Fluorescent Protein-expressing (RFP). Control animals receiving carrier medium without cells lost weight **(Fig. S10A)** and died within 3 weeks **(Fig. 3B, Table S1)**, developing cholestasis **(Fig. S10B)** and cholangiopathy demonstrated by IF **(Fig. S10C)**, histology **(Fig. S10D)** and Magnetic Resonance Cholangio-Pancreatography (MRCP) **(Fig. 3C, S11A-S11C, Movie S1-S6)**. On the contrary, animals receiving organoids were electively culled at the end of the experiment and survived for up to 3 months with resolution of cholangiopathy and normal serum biochemistry **(Fig. 3B-3C, S10A-S10B, S11B-S11C, Movie S3-S4, S6)**. The transplanted gallbladder cholangiocytes engrafted in various size intrahepatic ducts **(Fig. 3D, S12A-C, Movie S7-S9)** corresponding to ~25-55% of the regenerated biliary epithelium **(Fig. S12C),** and assumed an intrahepatic identity by losing gallbladder (SOX17) and expressing intrahepatic markers (SOX4, DCDC2, BICC1) **(Fig. 3D, Fig. S12A-S12B)**. Core biliary markers (KRT7, KRT19, CFTR) were also expressed **(Fig. S12A)**, while we observed YAP activation both in engrafted and native cells (**Fig. S12B, S12E)** in accordance with previous reports (*13*). Of note, we never observed expression of other hepatic lineage markers such as albumin indicating that cholangiocyte organoid plasticity is likely to be limited to their biliary lineage **(Fig. S12A)**. Furthermore, the engrafted cells expressed proliferation markers **(Fig. S12B, S12D)** at similar levels to native mouse cholangiocytes; while abnormal growth or tumour formation was never noticed in all the analyses performed (**Fig. 3C, 3D, S10D, S12A-S12B**), including T1 weighed body MR imaging at the end of the experiment (**Movie S1, S3**). Thus, organoid transplantation provides the healthy cells required to repair the damaged epithelium and rescue acute injury.

To ensure that animal rescue and resolution of cholangiopathy was specific to cholangiocyte organoids, we repeated the experiment using Mesenchymal Stem Cells (MSCs), as a different cell type known to provide anti-inflammatory effects following transplantation through paracrine signalling **(Fig. S13A-S13C)**. This experiment allowed us to explore if organoids are essential for duct regeneration and animal rescue; and if some of the observed effects could be attributed to paracrine signals which are not unique to our cells. In sum, MSCs failed to engraft (**Fig. S13C**) and rescue the transplanted animals, which exhibited no difference in survival compared to controls (P>0.05; **Fig. S13A**) and no resolution of cholestasis on serum biochemistry **(Fig. S13B)**. Consequently, cholangiopathy resolution is specific to the engraftment of cholangiocyte organoids; and although additional therapeutic effects of our cells through growth factor and cytokine secretion cannot be completely excluded, these effects are unique to cholangiocyte organoids.

We then explored if organoid culture is required to 'unlock' the cells' plasticity or if this reflects an inherent property of primary cholangiocytes. To achieve this, we transplanted primary gallbladder cholangiocytes **(Fig. S13A-S13C)** directly post isolation without *in vitro* culture. Under these conditions very few primary cholangiocytes engrafted in the mouse bile ducts **(Fig. S13C)** most likely due to the cumulative stress of isolation and transplantation; and failed to rescue the animals or resolve cholestasis **(Fig. S13A, S13B)**. Nonetheless, the engrafted cells expressed intrahepatic markers and lost expression of gallbladder markers **(Fig. S13C)**. In conclusion, cholangiocyte plasticity is not limited to organoids grown *in vitro*; however, organoid culture is necessary for the cholangiocytes to recover from the stress of isolation and for large scale expansion providing the cell numbers required for engraftment and biliary repair.

Finally, to ensure that our results are not specific to the intrahepatic compartment or gallbladder organoids, we used our established methodology (*3*) to transplant common bile duct-derived cholangiocyte organoids in the gallbladder of immunocompromised mice. The engrafted cells exhibited loss of common bile duct makers and upregulation of gallbladder

markers **(Fig. S14)**, confirming that our previous findings apply to different compartments of the biliary tree and to organoids of different origin. Taken together, these results establish that cholangiocytes from different regions of the biliary tree are interchangeable and suggest that extrahepatic cells can be used to repair acute intrahepatic duct injury.

Cell transplantation experiments in mouse models are extremely useful but are not always predictive of therapeutic outcome (*19*). Furthermore, the mouse liver microenvironment is different to human, raising the possibility that our results may not translate between species. To address these challenges, we developed a new model for cell-based therapy in human utilizing *ex vivo* organ perfusion (*20*). Ex-vivo Normothermic Perfusion (NMP) was developed to improve organ preservation and reduce ischaemia-reperfusion injury by circulating warm oxygenated blood through liver grafts prior to transplantation. Importantly, the biliary tree is particularly susceptible to ischaemia which results in duct damage (*21*, *22*). Low bile pH (< 7.5) during NMP is used as a predictor of this type of cholangiopathy (*23*).

To assess the therapeutic potential of our cells for repairing human bile ducts, RFP gallbladder organoids were injected in the intrahepatic ducts of deceased transplant donor livers (n=3) with a bile pH<7.5 at the start of the experiment, signifying ischaemic duct injury. The organs were perfused with oxygenated blood and nutrients at normal body temperature (*20*); **Fig. 4A-4B, S15A**) for up to 100 hours in order to maintain a near-physiological microenvironment. Importantly, the organoids were delivered in a terminal branch of the intrahepatic ducts under fluoroscopic guidance to minimize the area of distribution of the cells and maximize cell density **(Fig. S15B)**. At the end of the experiment, ultrasound imaging revealed no evidence of duct dilatation or obstruction **(Fig. S15C)**, while RFP-expressing cells were not detected in the perfusate by flow cytometry, confirming that the injected cells remained in the biliary compartment **(Fig. 4C)**. More importantly, the transplanted organoids engrafted in the intrahepatic biliary tree **(Fig. 4D, S16A)**, with RFP cells regenerating ~40-85% of the injected ducts (**Fig. 16B**); and expressing key biliary markers (KRT7, KRT19, CFTR, GGT). Furthermore, engrafted gallbladder organoids exhibited loss of gallbladder (SOX17) and

upregulation of intrahepatic (SOX4, BICC1, DCDC2) markers without differentiation to other hepatic lineages **(Fig. 4D, S15D, S16A-S16B)**. Thus, at the end of the experiment, the injected ducts consisted of a mixture of native and transplanted cholangiocytes (**Fig. S16A-S16B**), with multiple transition points between donor and recipient cells and no evidence of cholangiopathy **(Fig 4D, S15D, S16A)**.

Conversely, control ducts not receiving cells demonstrated evidence of ischaemic injury with loss of epithelial continuity and sloughing of cells in the duct lumen **(Fig. 4D)**. We subsequently characterised the impact of engraftment on organ function. Physiologically, cholangiocytes modify the composition and pH of bile through water transfer and bicarbonate secretion (*6*). Therefore, we compared the bile from organoid-injected vs. carrier-injected ducts. Accordingly, bile aspirated from ducts injected with cells exhibited higher pH and volume **(Fig. 4E)** confirming that transplanted cholangiocytes retain their function to modify bile composition. Together, these results provide the first proof-of-principle that perfused organs can be used to ascertain functional engraftment of human cells and validate our mouse data by showing that cholangiocytes are interchangeable for transplantation in human organs.

Our results show that the biliary epithelium is composed of cholangiocytes with diverse transcriptional profiles which are determined by their local environment. This diversity is lost in organoid culture due to the lack of niche stimuli. However, organoids can adapt appropriately to local environmental cues both *in vitro* and following transplantation, restore the expression of region-specific markers and assume different regional identities. Thus, organoids from a single region could potentially repair the entirety of the biliary tree. This plasticity could have significant implications for regenerative medicine. Indeed, although autologous cell-based therapy potentially avoids the need for immunosuppression its application for primary organoids is limited by the impact of disease on the epithelium. However, cholangiopathies belong to a family of localising diseases, affecting predominantly specific regions of an organ (*24*). Consequently, our results provide proof-of-concept that cholangiocytes from spared regions, such as the gallbladder, could be used for autologous

cell-based therapy to repair human intrahepatic bile ducts, which constitute the most common site of injury in cholangiopathies. Moreover, our novel model for cell engraftment in human perfused organs paves the road for the use of *ex vivo* cell-based therapy to improve graft function prior to transplantation, which could ultimately increase the number of useable organs and reduce pressure on the transplant waiting list. In this context, quality controlled and readily available allogeneic cholangiocyte organoids from a cell bank could be used routinely in the future to prevent ischaemic cholangiopathy in organs at risk of biliary injury (e.g. low bile pH), since the organ recipients will receive immunosuppression as part of their standard care. Importantly, our results provide proof-of-principle for the transplantation of organoids in human organs which could expedite regulatory approval and fast-tack first-in-man trials. Ultimately, the same approach could also be applied to a variety of *ex vivo* perfused organs and cell types to validate functional cell engraftment, demonstrate safety, improve cell transplantation technique and efficacy and accelerate clinical translation of new cell-based therapies.

References and notes

1. J. Drost, H. Clevers, Translational applications of adult stem cell-derived organoids. *Dev.* **144**, 968–975 (2017).

2. R. H. Squires, V. Ng, R. Romero, U. Ekong, W. Hardikar, S. Emre, G. V Mazariegos, Evaluation of the pediatric patient for liver transplantation: 2014 practice guideline by the American Association for the Study of Liver Diseases, American Society of Transplantation and the North American Society for Pediatric Gastroenterology, Hepatology and Nutrition. *Hepatology*. **60**, 362–98 (2014).

3. F. Sampaziotis, A. W. A. W. Justin, O. C. O. C. Tysoe, S. Sawiak, E. M. Godfrey, S. S. S. S. Upponi, R. L. R. L. Gieseck, M. C. M. C. De Brito, N. L. N. L. Berntsen, M. J. M. J. Gómez-Vázquez, D. Ortmann, L. Yiangou, A. Ross, J. Bargehr, A. Bertero, M. C. F. M. C. F. Zonneveld, M. T. M. T. Pedersen, M. Pawlowski, L. Valestrand, P. Madrigal, N. Georgakopoulos, N. Pirmadjid, G. M. G. M. Skeldon, J. Casey, W. Shu, P. M. P. M. Materek, K. E. K. E. Snijders, S. E. Brown, C. A. C. A. Rimland, I. Simonic, S. E. S. E. Davies, K. B. K. B. Jensen, M. Zilbauer, W. T. H. W. T. H. Gelson, G. J. G. J. Alexander, S. Sinha, N. R. F. N. R. F. Hannan, T. A. T. A. Wynn, T. H. T. H. Karlsen, E. Melum, A. E. A. E. Markaki, K. Saeb-Parsy, L. Vallier, Reconstruction of the mouse extrahepatic biliary tree using primary human extrahepatic cholangiocyte organoids. *Nat. Med.* **23**, 954–963 (2017).

4. K. Parikh, A. Antanaviciute, D. Fawkner-Corbett, M. Jagielowicz, A. Aulicino, C. Lagerholm, S. Davis, J. Kinchen, H. H. Chen, N. K. Alham, N. Ashley, E. Johnson, P. Hublitz, L. Bao, J. Lukomska, R. S. Andev, E. Björklund, B. M. Kessler, R. Fischer, R. Goldin, H. Koohy, A. Simmons, Colonic epithelial cell diversity in health and inflammatory bowel disease. *Nature*. **567**, 49–55 (2019).

5. C. A. Rimland, S. G. Tilson, C. M. Morell, R. A. Tomaz, W.-Y. Lu, S. E. Adams, N. Georgakopoulos, F. Otaizo-Carrasquero, T. G. Myers, J. R. Ferdinand, R. L. Gieseck,

F. Sampaziotis, O. C. Tysoe, B. Wesley, D. Muraro, G. C. Oniscu, N. R. Hannan, S. J. Forbes, K. Saeb-Parsy, T. A. Wynn, L. Vallier, Regional differences in human biliary tissues and corresponding *in vitro* derived organoids. *Hepatology* (2020), doi:10.1002/hep.31252.

6. J. H. Tabibian, A. I. Masyuk, T. V. Masyuk, S. P. O'Hara, N. F. LaRusso, Physiology of cholangiocytes. *Compr. Physiol.* **3**, 541–565 (2013).

7. A. I. Masyuk, N. F. LaRusso, Aquaporins in the hepatobiliary system. *Hepatology*. **43**, S75–S81 (2006).

8. K.-S. Yoo, H. S. Choi, D. W. Jun, H. L. Lee, O. Y. Lee, B. C. Yoon, K. G. Lee, S. S. Paik, Y. S. Kim, J. Lee, MUC Expression in Gallbladder Epithelial Tissues in Cholesterol-Associated Gallbladder Disease. *Gut Liver*. **10**, 851–8 (2016).

9. S. J. L. B. Zweers, K. A. C. Booij, M. Komuta, T. Roskams, D. J. Gouma, P. L. M. Jansen, F. G. Schaap, The human gallbladder secretes fibroblast growth factor 19 into bile: Towards defining the role of fibroblast growth factor 19 in the enterobiliary tract. *Hepatology*. **55**, 575–583 (2012).

10. Y. Zong, B. Z. Stanger, Molecular mechanisms of bile duct development. *Int. J. Biochem. Cell Biol.* **43**, 257–64 (2011).

11. K. Si-Tayeb, F. P. Lemaigre, S. A. Duncan, Organogenesis and Development of the Liver. *Dev. Cell*. **18**, 175–189 (2010).

12. N. Aizarani, A. Saviano, Sagar, L. Mailly, S. Durand, J. S. Herman, P. Pessaux, T. F. Baumert, D. Grün, A human liver cell atlas reveals heterogeneity and epithelial progenitors. *Nature*. **572**, 199–204 (2019).

13. B. J. Pepe-Mooney, M. T. Dill, A. Alemany, J. Ordovas-Montanes, Y. Matsushita, A. Rao, A. Sen, M. Miyazaki, S. Anakk, P. A. Dawson, N. Ono, A. K. Shalek, A. van Oudenaarden, F. D. Camargo, Single-Cell Analysis of the Liver Epithelium Reveals

Dynamic Heterogeneity and an Essential Role for YAP in Homeostasis and Regeneration. *Cell Stem Cell*. **25**, 23-38.e8 (2019).

14. L. Planas-Paz, T. Sun, M. Pikiolek, N. R. Cochran, S. Bergling, V. Orsini, Z. Yang, F. Sigoillot, J. Jetzer, M. Syed, M. Neri, S. Schuierer, L. Morelli, P. S. Hoppe, W. Schwarzer, C. M. Cobos, J. L. Alford, L. Zhang, R. Cuttat, A. Waldt, N. Carballido-Perrig, F. Nigsch, B. Kinzel, T. B. Nicholson, Y. Yang, X. Mao, L. M. Terracciano, C. Russ, J. S. Reece-Hoyes, C. Gubser Keller, A. W. Sailer, T. Bouwmeester, L. E. Greenbaum, J. J. Lugus, F. Cong, G. McAllister, G. R. Hoffman, G. Roma, J. S. Tchorz, YAP, but Not RSPO-LGR4/5, Signaling in Biliary Epithelial Cells Promotes a Ductular Reaction in Response to Liver Injury. *Cell Stem Cell*. **25**, 39-53.e10 (2019).

15. A. Lanzini, BILE. *Encycl. Food Sci. Nutr.*, 471–478 (2003).

16. O. C. Tysoe, A. W. Justin, T. Brevini, S. E. Chen, K. T. Mahbubani, A. K. Frank, H. Zedira, E. Melum, K. Saeb-Parsy, A. E. Markaki, L. Vallier, F. Sampaziotis, Isolation and propagation of primary human cholangiocyte organoids for the generation of bioengineered biliary tissue. *Nat. Protoc.* **14**, 1884–1925 (2019).

17. M.-O. Lee, J. H. Kim, B.-I. Yoon, S.-B. Kwon, K.-S. Kang, M. Kim, G. Kong, J.-W. Hwang, B.-H. Lee, H.-L. Kim, J.-Y. Yi, J.-S. Park, H. Chung, Time- and Dose-based Gene Expression Profiles Produced by a Bile-duct–damaging Chemical, 4,4′-methylene Dianiline, in Mouse Liver in an Acute Phase. *Toxicol. Pathol.* **36**, 660–673 (2008).

18. N. L. Berntsen, B. Fosby, L. Valestrand, C. Tan, H. M. Reims, E. Schrumpf, T. H. Karlsen, P. D. Line, E. Melum, Establishment of a surgical bile duct injection technique giving direct access to the bile ducts for studies of the murine biliary tree. *Am. J. Physiol. - Gastrointest. Liver Physiol.* **314**, G349–G359 (2018).

19. C. Arber, M. K. Brenner, P. Reddy, Mouse models in bone marrow transplantation and adoptive cellular therapy. *Semin. Hematol.* **50**, 131–144 (2013).

20. D. Nasralla, C. C. Coussios, H. Mergental, M. Z. Akhtar, A. J. Butler, C. D. L. Ceresa, V. Chiocchia, S. J. Dutton, J. C. García-Valdecasas, N. Heaton, C. Imber, W. Jassem, I. Jochmans, J. Karani, S. R. Knight, P. Kocabayoglu, M. Malagò, D. Mirza, P. J. Morris, A. Pallan, A. Paul, M. Pavel, M. T. P. R. Perera, J. Pirenne, R. Ravikumar, L. Russell, S. Upponi, C. J. E. Watson, A. Weissenbacher, R. J. Ploeg, P. J. Friend, A randomized trial of normothermic preservation in liver transplantation. *Nature*. **557**, 50–56 (2018).

21. A. I. Skaro, C. L. Jay, T. B. Baker, E. Wang, S. Pasricha, V. Lyuksemburg, J. A. Martin, J. M. Feinglass, L. B. Preczewski, M. M. Abecassis, The impact of ischemic cholangiopathy in liver transplantation using donors after cardiac death: The untold story. *Surgery*. **146**, 543–553 (2009).

22. C. K. Enestvedt, S. Malik, P. P. Reese, A. Maskin, P. S. Yoo, S. A. Fayek, P. Abt, K. M. Olthoff, A. Shaked, Biliary complications adversely affect patient and graft survival after liver retransplantation. *Liver Transpl.* **19**, 965–72 (2013).

23. C. J. E. Watson, V. Kosmoliaptsis, C. Pley, L. Randle, C. Fear, K. Crick, A. E. Gimson, M. Allison, S. Upponi, R. Brais, I. Jochmans, A. J. Butler, Observations on the ex situ perfusion of livers for transplantation. *Am. J. Transplant*. **18**, 2005–2020 (2018).

24. R. G. Farmer, W. A. Hawk, R. B. Turnbull, Farmer, R. G., Hawk, W. A. and Turnbull, R. B. (1975) ‘Clinical patterns in Crohn’s disease: a statistical study of 615 cases.’, Gastroenterology, 68(4 Pt 1), pp. 627–35. Available at: http://www.ncbi.nlm.nih.gov/pubmed/1123132 (Accessed: 11 September 201. *Gastroenterology*. **68**, 627–35 (1975).

25. S. A. MacParland, J. C. Liu, X. Z. Ma, B. T. Innes, A. M. Bartczak, B. K. Gage, J. Manuel, N. Khuu, J. Echeverri, I. Linares, R. Gupta, M. L. Cheng, L. Y. Liu, D. Camat, S. W. Chung, R. K. Seliga, Z. Shao, E. Lee, S. Ogawa, M. Ogawa, M. D. Wilson, J. E.

Fish, M. Selzner, A. Ghanekar, D. Grant, P. Greig, G. Sapisochin, N. Selzner, N. Winegarden, O. Adeyi, G. Keller, G. D. Bader, I. D. McGilvray, Single cell RNA sequencing of human liver reveals distinct intrahepatic macrophage populations. *Nat. Commun.* **9**, 4383 (2018).

26. D. J. McCarthy, K. R. Campbell, A. T. L. Lun, Q. F. Wills, Scater: pre-processing, quality control, normalization and visualization of single-cell RNA-seq data in R. *Bioinformatics*. **33**, 1179–1186 (2017).

27. A. Butler, P. Hoffman, P. Smibert, E. Papalexi, R. Satija, Integrating single-cell transcriptomic data across different conditions, technologies, and species. *Nat. Biotechnol.* **36**, 411–420 (2018).

28. L. Haghverdi, A. T. L. Lun, M. D. Morgan, J. C. Marioni, Batch effects in single-cell RNA-sequencing data are corrected by matching mutual nearest neighbors. *Nat. Biotechnol.* **36**, 421–427 (2018).

29. F. A. Wolf, P. Angerer, F. J. Theis, SCANPY: Large-scale single-cell gene expression data analysis. *Genome Biol.* **19** (2018), doi:10.1186/s13059-017-1382-0.

30. L. Haghverdi, M. Büttner, F. A. Wolf, F. Buettner, F. J. Theis, Diffusion pseudotime robustly reconstructs lineage branching. *Nat. Methods*. **13**, 845–848 (2016).

31. X. Qiu, Q. Mao, Y. Tang, L. Wang, R. Chawla, H. A. Pliner, C. Trapnell, Reversed graph embedding resolves complex single-cell trajectories. *Nat. Methods*. **14**, 979–982 (2017).

32. V. Y. Kiselev, K. Kirschner, M. T. Schaub, T. Andrews, A. Yiu, T. Chandra, K. N. Natarajan, W. Reik, M. Barahona, A. R. Green, M. Hemberg, SC3: Consensus clustering of single-cell RNA-seq data. *Nat. Methods*. **14**, 483–486 (2017).

33. L. Zappia, A. Oshlack, Clustering trees: a visualization for evaluating clusterings at multiple resolutions. *Gigascience*. **7** (2018), doi:10.1093/gigascience/giy083.

34. A. Subramanian, P. Tamayo, V. K. Mootha, S. Mukherjee, B. L. Ebert, M. A. Gillette, A. Paulovich, S. L. Pomeroy, T. R. Golub, E. S. Lander, J. P. Mesirov, Gene set enrichment analysis: A knowledge-based approach for interpreting genome-wide expression profiles. *Proc. Natl. Acad. Sci. U. S. A.* **102**, 15545–15550 (2005).

35. M. V. Kuleshov, M. R. Jones, A. D. Rouillard, N. F. Fernandez, Q. Duan, Z. Wang, S. Koplev, S. L. Jenkins, K. M. Jagodnik, A. Lachmann, M. G. McDermott, C. D. Monteiro, G. W. Gundersen, A. Ma'ayan, Enrichr: a comprehensive gene set enrichment analysis web server 2016 update. *Nucleic Acids Res.* **44**, W90–W97 (2016).

36. F. Sampaziotis, M. C. De Brito, P. Madrigal, A. Bertero, K. Saeb-Parsy, F. a C. F. A. C. Soares, E. Schrumpf, E. Melum, T. H. T. H. Karlsen, J. A. A. Bradley, W. T. H. W. T. H. Gelson, S. Davies, A. Baker, A. Kaser, G. J. G. J. Alexander, N. R. F. N. R. F. Hannan, L. Vallier, M. Cardoso de Brito, P. Madrigal, A. Bertero, K. Saeb-Parsy, F. a C. F. A. C. Soares, E. Schrumpf, E. Melum, T. H. T. H. Karlsen, J. A. A. Bradley, W. T. H. W. T. H. Gelson, S. Davies, A. Baker, A. Kaser, G. J. G. J. Alexander, N. R. F. N. R. F. Hannan, L. Vallier, Cholangiocytes derived from human induced pluripotent stem cells for disease modeling and drug validation. *Nat. Biotechnol.* **33**, 845–852 (2015).

37. F. Sampaziotis, M. C. de Brito, I. Geti, A. Bertero, N. R. Hannan, L. Vallier, Directed differentiation of human induced pluripotent stem cells into functional cholangiocyte-like cells. *Nat. Protoc.* **12**, 814–827 (2017).

38. R. Ravikumar, W. Jassem, H. Mergental, N. Heaton, D. Mirza, M. T. P. R. Perera, A. Quaglia, D. Holroyd, T. Vogel, C. C. Coussios, P. J. Friend, Liver Transplantation After Ex Vivo Normothermic Machine Preservation: A Phase 1 (First-in-Man) Clinical Trial. *Am. J. Transplant.* **16**, 1779–1787 (2016).

Acknowledgements:

The authors would like to thank A. Petrunkina and the NIHR Cambridge BRC Cell Phenotyping Hub for their help with flow cytometry and cell sorting; K Burling and the MRC MDU Mouse Biochemistry Laboratory [MRC_MC_UU_12012/5] for processing mouse serum samples; the Cambridge Biorepository for Translational Medicine for the provision of human tissue used in the study, Pedro Madrigal and Chichau Miau for bioinformatic support; Carlos Costa for his help with the NMP experiments; Kate Reid and Rachel Clarke for their help with radiological imaging during NMP experiments; Peter Humphreys, Darran Clements and Simon McCallum for their help with confocal imaging. The monoclonal antibody TROMA-III developed by R Kemler was obtained from the Developmental Studies Hybridoma Bank, created by the NICHD of the NIH and maintained at The University of Iowa, Department of Biology, Iowa City, IA 52242.

Funding: F.S. was supported by an NIHR Clinical Lectureship, the Academy of Medical Sciences Starter Grant for Clinical Lecturers, the Addenbrooke's Charitable Trust and the Rosetrees Trust. T.B. was supported an EASL Juan Rodes fellowship. The L.V. lab is funded by the ERC advanced grant New-Chol, the Cambridge University Hospitals National Institute for Health Research Biomedical Research Centre and the core support grant from the Wellcome Trust and Medical Research Council of the Wellcome–Medical Research Council Cambridge Stem Cell Institute. L.G. and Sa.S were supported by a BHF Senior Research Fellowship (FS/18/46/33663).

Author contributions: F.S. conceived and designed the study, performed experiments, acquired, interpreted and analysed the data, developed and validated the protocols described, performed bioinformatic analysis, generated the figures, wrote and edited the manuscript. D.M. Performed bioinformatics analysis. O.C.T. contributed to cell culture, harvesting and processing of tissue, single-cell RNA sequencing (scRNAseq) experiments and animal experiments. T.E.B. contributed to animal experiments. St.S. performed the Magnetic Resonance Imaging (MRI) experiments. E.M.G. performed the 3D reconstruction of the mouse

biliary tree from MRI images. E.M.G. and S.S.U. reviewed and reported the MRI images. T.B. contributed to tissue culture, QPCR, immunofluorescence, tissue clarification and wholemount staining experiments. B.T.W. contributing to tissue dissociation and scRNAseq experiments. J.G.B. contributed to scRNAseq experiments. K.M. contributed to primary tissue harvesting tissue. Gi.C. contributed to scRNAseq experiments, flow cytometry and magnetic associated cell sorting. R.L.G. contributed to animal experiments, IF, and tissue histology. N.L.B. contributed to animal experiments. V.L.M. contributed to harvesting primary tissue. K.C., C.F., S.R, L.S. contributed to ex-vivo normothermic perfusion (NMP) experiments. J.B. contributed to imaging. L.G. contributed to tissue clarification and wholemount staining experiments as well as critical review of this data. D.O. and A.O. contributed to flow cytometry analyses and contributed through critical revision of the manuscript for important intellectual content. P. H. contributed to 3D reconstruction and rendering of immunofluorescence images. S.E.B. contributed to experimental design and critical revision of the manuscript for important intellectual content. Ga.C provided primary human samples. S. E. D. reviewed and reported the histology images and contributed through critical revision of the manuscript for important intellectual content. I.A. contributed to bile aspiration using microdialysis catheters. A.J.B., C.J.E.W. contributed to NMP experiments and critical revision of the manuscript for important intellectual content. T.C.S performed fluoroscopic cannulation of peripheral ducts in NMP experiments and contributed through critical revision of the manuscript for important intellectual content. M.P.M., W.T.H.G, G.F.M, Sa.S, S.T., P.G., E.M. contributed through critical revision of the manuscript for important intellectual content. K.S.-P. provided primary tissue, performed animal and ex-vivo normothermic perfusion experiments, contributed to the design and concept of study, interpreted the data and edited the manuscript. L.V. Designed and conceived the study, interpreted the data, wrote and edited the manuscript. All the authors approved the manuscript.

Competing interests: FS, KSP and LV are founders and shareholders of BILITECH. LV is a founder and shareholder of DEFINIGEN. The remaining authors have no competing interests to disclose.

Data and materials availability: All data is available in the main text or the supplementary materials. Single-cell RNA sequencing data are available on ArrayExpress. Accession number: E-MTAB-8495

Supplementary Materials:

Materials and Methods

Figures S1 to S16

Tables S1 to S3

Movies S1 to S9

Data S1 to S3

References (*25*, *26*, *35–38*, *27–34*)

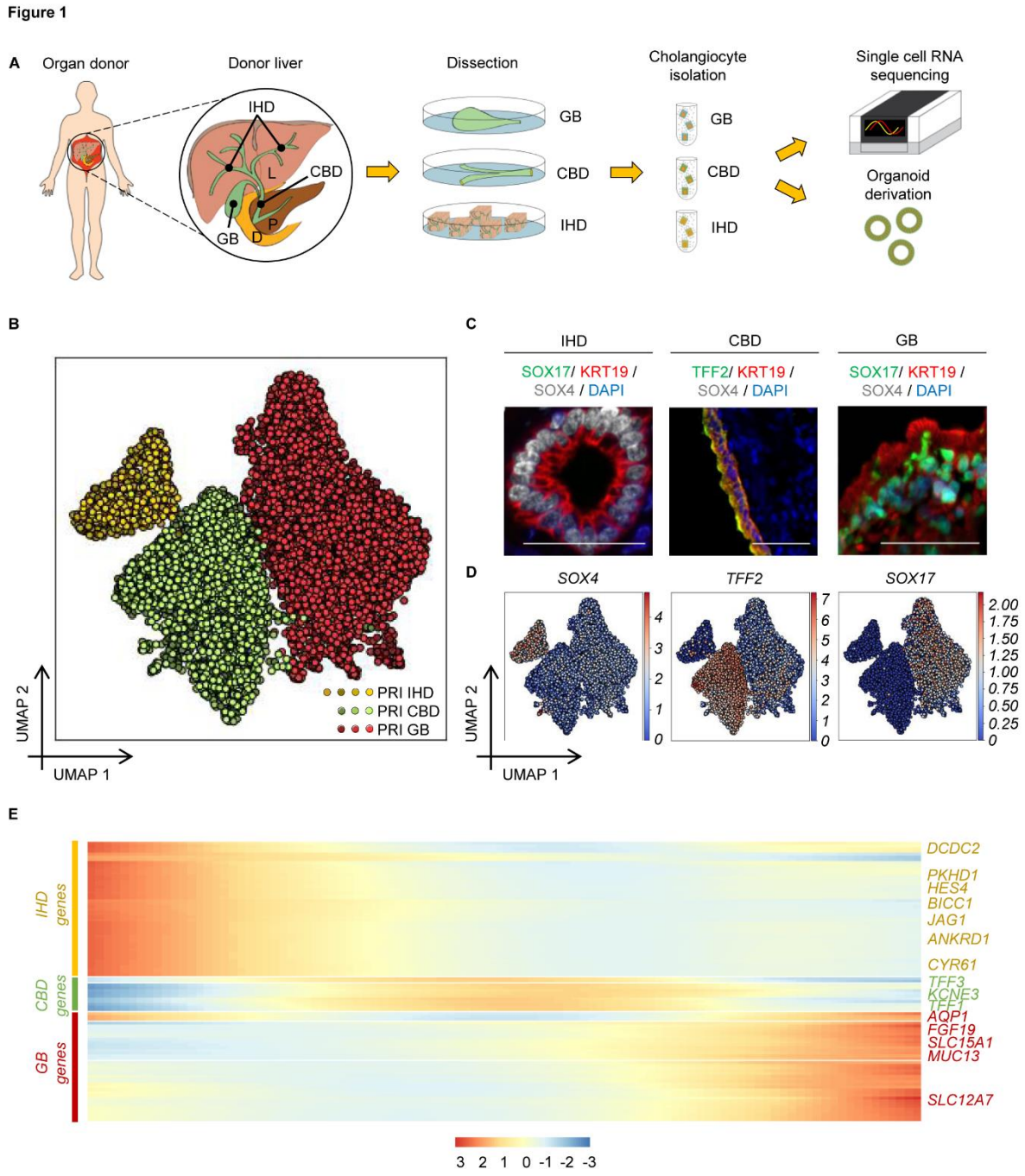

Fig. 1. Transcriptional profiling of primary cholangiocytes. (**A**) Schematic representation of the methodology used for single cell RNA sequencing (scRNAseq). (**B**) UMAP plot (7295 primary cells, n=10 individuals) illustrating distinct primary cholangiocyte populations in different regions of the biliary tree. (**C-D**) Immunofluorescence images (**C**) and UMAP

representation of normalized gene expression (**D**) of primary cholangiocytes illustrating differential expression of representative region markers. Scale bars: 50μm. (**E**) Heatmap of top 100 differentially expressed genes (DEGs) in pseudotime (**Data S2**) demonstrating a gradual transition in the transcriptional profile of cholangiocytes between different regions of the biliary tree. PRI, Primary; IHD, IntraHepatic Ducts; CBD, Common Bile Duct; GB, Gallbladder; P, Pangreas; D, Duodenum.

Figure 2

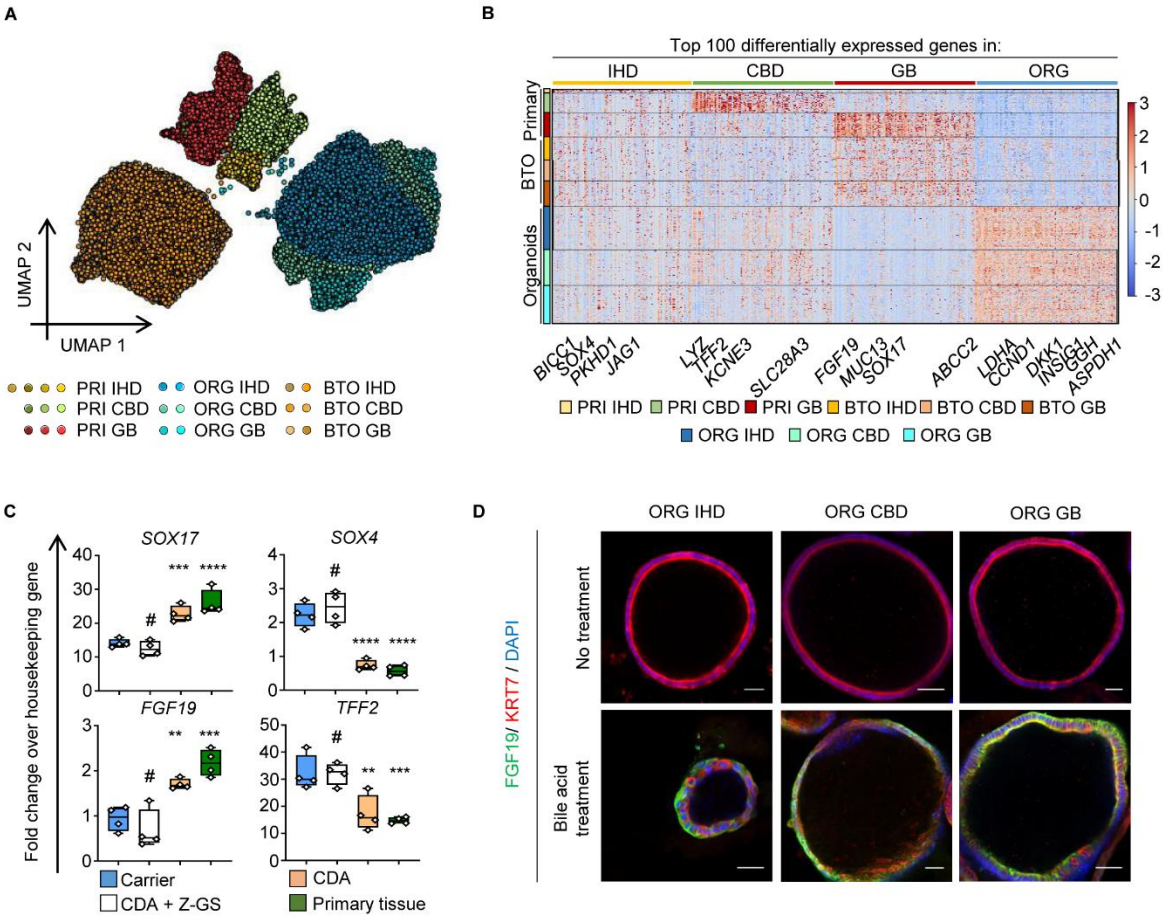

Fig. 2. Cholangiocyte Organoid (CO) identity is controlled by niche stimuli. (**A**) UMAP (35,603 cells) of primary cholangiocytes and their corresponding organoids before and after gallbladder bile treatment, illustrating similarities between different region organoids and changes in their signature in response to bile. PRI, Primary; IHD, IntraHepatic Ducts; CBD, Common Bile Duct; GB, Gallbladder; ORG, Organoids; BTO, Bile-Treated Organoids. (**B**) Heatmap of top 100 Differentially Expressed Genes (DEGs) between primary regions, organoids and BTOs (**Data S1-S2**), illustrating that organoids lose regional differences and upregulate culture-related genes, but re-acquire gallbladder markers following bile treatment. (**C-D**) QPCR (**C**) (n=4 samples per group; center line, median; box, interquartile range (IQR); whiskers, range; housekeeping gene, *HMBS*; #*P*>0.05, ***P*<0.01, ****P*<0.001, *****P*<0.0001);

and immunofluorescence (**D**) demonstrating upregulation of gallbladder markers and bile acid target genes following treatment with chenodeoxycholic acid (CDA), in the absence of the FXR inhibitor Z-GS. Z-GS, Z-guggulsterone. Scale bars, 50μm.

Figure 3

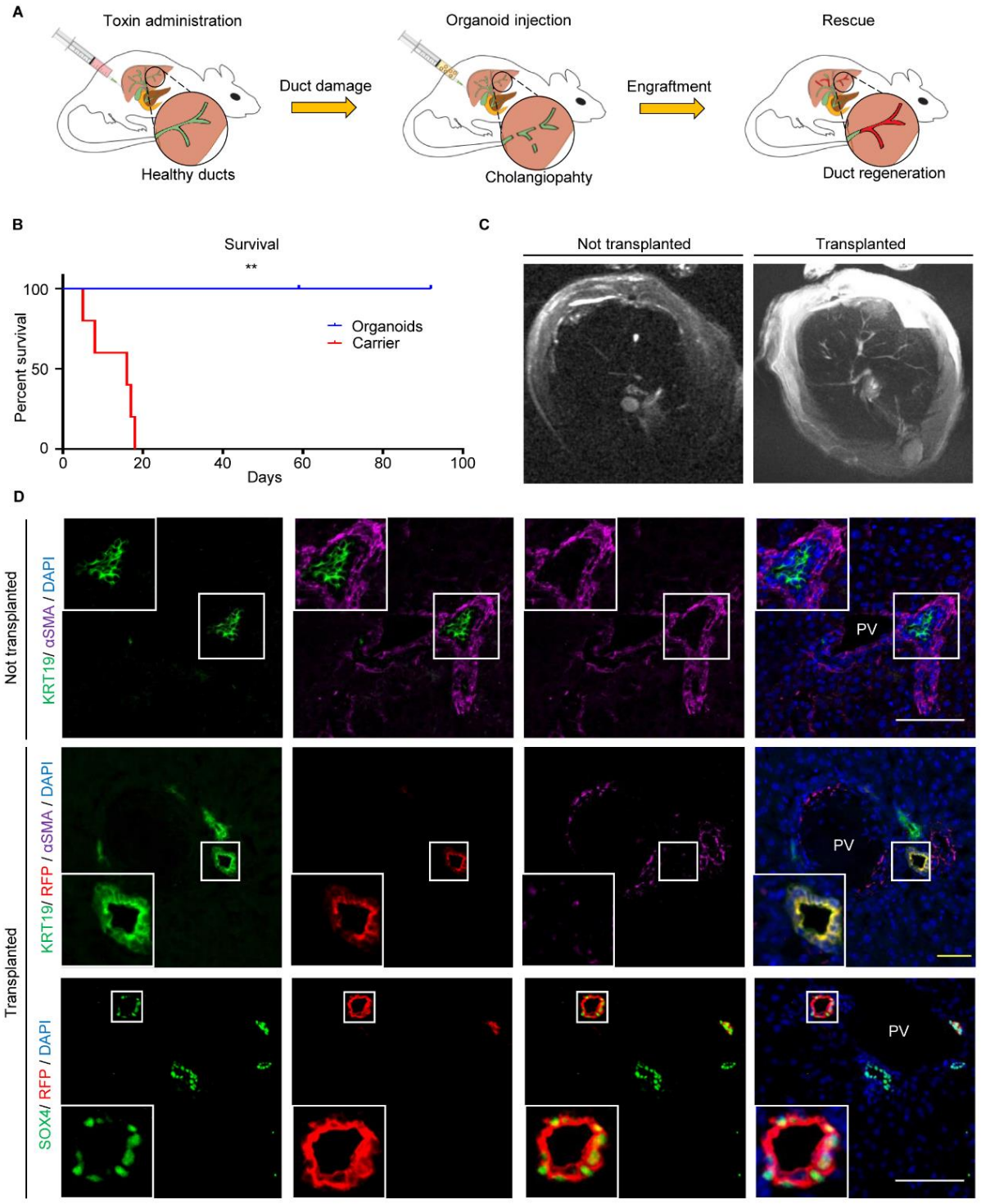

Fig. 3. Cholangiocyte organoids (COs) rescue cholangiopathy following transplantation and assume an identity corresponding to the site of engraftment. (**A**) Experimental outline schematic. (**B**) Kaplan-Meier curve (**Table S1**: number of animals at risk)

demonstrating animal rescue following gallbladder organoids injection; *P*=0.0018(**), log-rank test. (**C**) Magnetic Resonance Cholangiopancreatography (MRCP) demonstrating rescue of cholangiopathy following organoid injection. (**D**) Immunofluorescence demonstrating engraftment of Red Fluorescent Protein (RFP)-expressing gallbladder organoids in portal triads, with upregulation of intrahepatic (SOX4) markers. Scale bars; yellow, 50μm; white, 100μm. PV, portal vein.

Figure 4

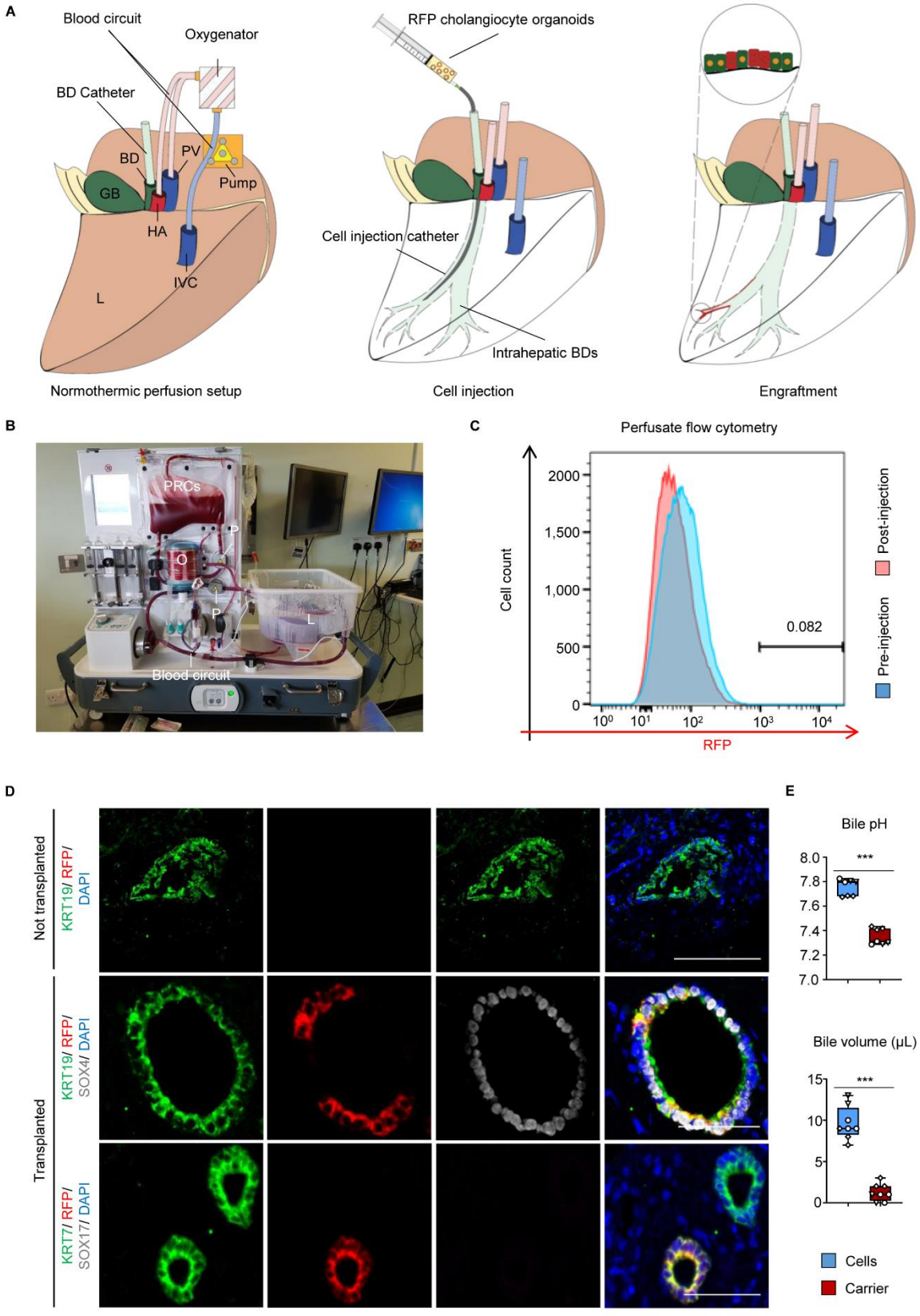
A
Blood circuit
Oxygenator
BD Catheter
BD
PV
Pump
GB
HA
IVC
L
Normothermic perfusion setup
RFP cholangiocyte organoids
Cell injection catheter
Intrahepatic BDs
Cell injection
Engraftment
B
PRCs
O
P
A
P
L
Blood circuit
C
Perfusate flow cytometry
Cell count
2000
1,500
1,000
500
0
0.082
Post-injection
Pre-injection
RFP
D
Not transplanted
KRT19/ RFP/ DAPI
Transplanted
KRT19/ RFP/ SOX4/ DAPI
KRT7/ RFP/ SOX17/ DAPI
E
Bile pH
***
8.0
7.8
7.6
7.4
7.2
7.0
Bile volume (µL)
***
15
10
5
0
Cells
Carrier

1

2

Fig. 4. Cholangiocyte organoids (COs) engraft in a human liver receiving Normothermic Perfusion (NMP) and improve bile properties. (**A**) Schematic representation of the technique for organoid injection and (**B**) photograph of the NMP circuit used. BD, Bile Duct; GB, Gallbladder; HA, Hepatic Artery; PV, Portal Vein; IVC, Inferior Vena Cava; L, Liver RFP, Red Fluorescent Protein; P, pump; O, oxygenator; PRC, Packed Red Cells. (**C**) Flow cytometry revealing absence of RFP cells in the perfusate. (**D**) Immunofluorescence revealing engraftment of RFP gallbladder organoids with upregulation of intrahepatic (SOX4) and loss of gallbladder (SOX17) markers. Scale bars, 50μm. (**E**) Organoid injection improves bile pH and choleresis. ***P<0.001. N=3 NMP livers. Each measurement is represented by a different data point, each organ is represented by a different symbol.

Science
AAAS

Supplementary Materials for

Cholangiocyte organoids can repair bile ducts after transplantation in human liver

Fotios Sampaziotis[*], Daniele Muraro, Olivia C. Tysoe , Stephen Sawiak, Timothy E. Beach, Edmund M. Godfrey, Sara S. Upponi, Teresa Brevini, Brandon T. Wesley, Jose Garcia-Bernando, Krishnaa Mahbubani, Giovanni Canu, Richard Gieseck III, Natalie L. Berntsen, Victoria L. Mulcahy, Keziah Crick, Corrina Fear, Sharayne Robinson, Lisa Swift, Laure Gambardella, Johannes Bargehr, Daniel Ortmann, Stephanie E. Brown, Anna Osnato, Michael Murphy, Gareth Corbett, William T. H. Gelson, George F. Mells, Peter Humphreys, Susan E. Davies, Irum Amin, Paul Gibbs, Sanjay Sinha, Sarah Teichmann, Andrew J Butler, Teik Choon See, Espen Melum, Christopher J. E. Watson, Kourosh Saeb-Parsy[†], Ludovic Vallier[†*]

[†]These authors share senior authorship

[*]Correspondence to: fs347@cam.ac.uk; lv225@cam.ac.uk

This PDF file includes:

Materials and Methods
Figs. S1 to S16
Tables S1 to S3
Captions for Movies S1 to S9
Captions for Data S1 to S3

Other Supplementary Materials for this manuscript include the following:

Movies S1 to S9
Movie S1: Movie S1 Carrier1 T1.mp4
Movie S2: Movie S2 Carrier1 T2.mp4
Movie S3: Movie S3 Cells1 T1.mp4
Movie S4: Movie S4 Cells1 T2.mp4
Movie S5: Movie S5 MR 3D reconstruction Carrier.mp4
Movie S6: Movie S6 MR 3D reconstruction Cells.mp4
Movie S7: Movie S7 Z-stack KRT19(GREEN)-RFP(RED).avi
Movie S8: Movie S8 3D reconstruction KRT19(GREEN)-RFP(RED).mp4
Movie S9: Movie S9 3D rendering KRT19(GREEN)-RFP(RED).mp4

Data S1 to S3
Data S1: Data S1 Differentially Expressed Genes in Primary Cholangiocytes.xlsx

Data S2: Data S2 Differentially Expressed Genes in Pseudotime.xlsx
Data S3: Data S2 Differentially Expressed Genes between organoids and primary cholangiocytes.xlsx

Materials and Methods

Ethical approval

Gallbladder, bile duct, liver biopsy and bile samples were obtained from deceased organ donors (National Research Ethics Committee East of England – Cambridge South 15/EE/0152). Human livers retrieved for transplantation but subsequently declined were used for ex vivo administration of cholangiocytes (National Research Ethics Committee East of England – Cambridge East 14/EE/0137). All human tissue was used after obtaining informed consent for use in research.

Tissue collection

Gallbladder, bile duct, liver biopsies and bile were obtained under sterile conditions from deceased transplant organ donors as rapidly as possible after cessation of circulation. Tissue samples, and liver retrieved for transplantation but subsequently declined, were transferred to the laboratory at 4°C in University of Wisconsin (UW®) organ presentation solution.

Tissue dissociation

Resected tissue (gallbladder, extrahepatic ducts and liver) was transferred to the lab as described above and processed immediately after resection. Gallbladder and extrahepatic bile duct samples were drained of bile and the organ lumen was exposed through a longitudinal incision. Liver samples were divided into $1cm^2$ cubes prior to processing. All samples were washed twice with warm PBS with $Ca^{2+}Mg^{2+}$ +EDTA (0.5mM), followed by enzymatic digestion with using Liberase (0.2 Wünsch/ml) in an incubated shaker at 37ºC and 200 RPM for 30 minutes. DNAse I (2000 U/ml) was added to the solution to prevent cell clumping and increase viability. Liver samples were dissociated further using the Miltenyi Biotec GentleMACS tissue dissociator and GentleMacs Tissue Dissociation C Tubes. For the gallbladder and extrahepatic duct samples, gentle mechanical scrapping of the lumen was adequate to release the epithelial cells following enzymatic digestion. All cell suspensions were filtered through 70um filters to remove debris and remaining tissue, washed with PBS containing 1% BSA (W/V) and centrifuged at 400g, for 5mins in a refrigerated centrifuge maintaining a temperature of 4ºC. The cells were resuspended in Miltenyi Biotec red blood cell (RBC) lysis and incubated for 10 minutes at room temperature (RT). The Miltenyi Biotec Debris Removal solution kit was used according to the manufacturer's instructions to remove remaining debris and dead cells. For liver samples, the resulting cell suspensions were centrifuged at 50g for 5 minutes (4ºC) to pellet the hepatocyte fraction, the supernatant was collected and cholangiocytes were isolated as described below.

Cell isolation

Following tissue dissociation to single cells, cholangiocytes were isolated with Magnetic Associated Cell Sorting (MACS) using the Miltenyi Biotech autoMACS Pro separator and CD326 (EpCAM) MicroBeads according to the manufacturer's instructions. The resulting cells were counted, centrifuged at 444g for 5 minutes, resuspended to a concentration of 1000 cells/ μL and stored on ice.

10x Single Cell Library Making Process

GEM-RTs (Gel-beads-in-emulsion which barcode the ploy adenylated mRNAs, followed by Reverse Transcription) were broken and Silane magnetic beads are used to purify first stand cDNA from the GEM-RT mixture and the cDNA was then amplified via PCR. Enzymatic fragmentation, end-repair and A-tailing were followed by size selection (using SPRISelect reagent). An adapter was ligated to the fragments and following a clean-up step, index PCR

took place. After a further round of size selection with SRISelect, completed libraries were quantified, (Agilent Bioanalyser and qPCR) and diluted for running on an Illumina sequencing instrument (HS4000).

Processing and normalization of 10X data

The results from the sequencing runs were checked manually to confirm that the overall yield and quality were as expected. The data from the instrument were converted to fastq format, the input format required by the 10X software cellranger, and aligned using the human reference GRCh36-1.2.0 available from 10X. The dataset was augmented by integrating counts of a cluster of cholangiocytes from a published dataset (cluster 17 in MacParland SA et al, 2018) (17). Cells were annotated as part of different origins, these being primary tissue (PRI), untreated organoids (ORG), treated organoids (ORGT). Each origin comprises three regions: intrahepatic duct (IHD), common bile duct (CBD), gallbladder (GB). The number of cells in each origin and region are reported in **Figure S1C**. Genes with read counts > 0 in at least 3 cells from each batch in at least one origin were maintained for downstream analysis. Low quality cells were removed based on the percentage of UMI mapping to the mitochondrial genome and the number of genes detected by determining outliers (3 median-absolute-deviations) with the routine isOutlier in the package scater (18). Cholangiocytes were isolated by retaining cells expressing at least one of the biliary markers EPCAM, KRT7, KRT19 (with number of counts > 3). Normalization, identification of highly variable genes and cell cycle regression (regressing out the difference between the G2M and S phase scores) were performed with the Seurat package (19). We employed the routine fastMNN in scran for batch correction (20). Batch corrected samples are shown in **figure 2A**. Small clusters derived by applying the Louvain method for community detection and characterized by cells which were outliers in the percentage of UMI mapping to the mitochondrial genome and the number of genes detected were filtered out.

Analysis of normalized 10X data

The normalized data were clustered using the Louvain method in the Scanpy package (21) by selecting a resolution which generated 3 clusters and with 10 random initialisations. Similarity between Louvain clusters and origin annotations was assessed using the Adjusted Rand Index (ARI) and the Adjusted Mutual Information (AMI). Both measures lie in the interval [0,1], where a value close to 0 indicates random labelling and exactly 1 means that the two partitions are identical. The average value calculated on the different partitions obtained by random initializations was > 0.95 for both measures, indicating a high correspondence between origins and clusters (**Fig. S5A**). The same analysis performed on regions showed poor matching between regions and clusters, suggesting similarity in the transcriptional profile of cells located in different regions (**Fig. S5A-B**). Transcriptional similarity was quantified at origin and region resolution by estimating the connectivity of data manifold partitions within the partition-based graph abstraction (PAGA) framework. At the origin resolution, this analysis notably highlighted higher transcriptional similarity between treated organoids and primary tissue than between untreated organoids and primary tissue (**Fig. S9B**). Interestingly, at the region resolution we identified higher transcriptional similarity between adjacent locations in primary tissues, with intrahepatic duct and gallbladder having the lowest connectivity value. This association between connectivity and anatomical location, together with the similarity of cells located in different regions, suggested a gradual variation in the transcriptional profile of cells in primary tissue that could be represented as a pseudo-spatial dimension. In this view, we analyzed the primary tissue by applying two methods for pseudo-temporal (or pseudo-spatial) ordering: diffusion pseudo-time (22) and Monocle 2 (23). In Monocle 2 differential expression in pseudotime was calculated using the differential GeneTest routine. Both methods

confirmed an association between transcriptional similarity and anatomical location, as highlighted by the density plot in **Figure S4B** and allowed the representation of regional markers along a pseudo-spatial dimension (**Fig. S4C**). Since the majority of cells had a diffusion pseudotime value >0.65 the density plot if figure **S4B** is shown in the range [0.65,0.9] to improve visualization and avoid overcrowding. We then analyzed each region individually in organoids (treated and untreated) and primary tissue to identify potential subpopulations of cells. Due to the relatively small sample sizes, we applied the clustering method SC3, whose high accuracy and robustness is derived combining multiple clustering solutions through a consensus approach (24). SC3 allows the user to pre-define the number of clusters. Because of the arbitrariness of this choice we varied the number of clusters between 1 and 10, calculated the stability of clusters across resolutions (SC3 stability index) and built a clustering tree showing how cells move as the clustering resolution is increased (package clustree), (25). As shown in **Figure S5C**, no stable sub-trees were formed within each region, indicating absence of stable clusters defining subpopulations of cells.

Regional markers and differentially expressed genes were identified by applying the Wilcoxon-Rank-Sum test (p-value<0.01, |log2 fold change| > 1) in Scanpy. Gene set, gene ontology and pathway enrichment were performed using the packages GSEA (26) and Enrichr (27).

Data availability

10X raw data (fastq files) have been deposited in the repository ArrayExpress with the accession number E-MTAB-8495

Organoid derivation and culture

A portion of the cells isolated for scRNAseq was cultured and propagated as organoids using our established methodology (11, 12). Cells were cultured under the same conditions irrespective of their region of origin.

Immunofluorescence, RNA extraction and Quantitative Real Time PCR

IF, RNA extraction and QPCR were performed as previously described (11, 12, 28, 29). A complete list of the primary and secondary antibodies used is provided in **table S2**. A complete list of the primers used is provided in **table S3**.

All QPCR data are presented as the median, interquartile range (IQR) and range (minimum to maximum) of four independent lines unless otherwise stated. Values are relative to the housekeeping gene Hydroxymethylbilane Synthase (HMBS).

All IF images were acquired using a Zeiss Axiovert 200M inverted microscope or a Zeiss LSM 700 confocal microscope. Imagej 1.48k software (Wayne Rasband, NIHR, USA, http://imagej.nih.gov/ij) was used for image processing. IF images are representative of 3 different experiments.

GGT activity

GGT activity was measured in triplicate using the MaxDiscovery™ gamma-Glutamyl Transferase (GGT) Enzymatic Assay Kit (Bioo scientific) based on the manufacturer's instructions. Error bars represent SD.

Alkaline Phosphatase staining

Alkaline phosphatase was carried out using the BCIP/NBT Color Development Substrate (5-bromo-4-chloro-3-indolyl-phosphate/nitro blue tetrazolium) (Promega) according to the manufacturer's instructions.

Flow cytometry analyses

Flow cytometry analyses were performed as previously described (11, 12, 28, 29).

Bile acid treatment

Organoids were incubated for 72 hours with 10μM CDA (Sigma, C9377-5G) in the presence or absence of 10μM Z-GS (Santa Cruz, sc-204414).

Animal experiments

All animal experiments were performed in accordance with UK Home Office regulations (UK Home Office Project License number PPL 70/8702). Immunodeficient NSG mice (NOD.Cg-Prkdcscid Il2rgtm1Wjl/SzJ), which lack B, T and NK lymphocytes, were bred in house, and food and water were available ad libitum before and after procedures. Male animals aged 4–8 weeks were used. Animals were assigned randomly to treatment and control groups. Experiments were performed blinded, and where this was not possible (e.g., due to performance of a surgical procedure), data were analysed blinded to the identity of the experimental groups. Littermate animals were used as controls.

Cell delivery

Cholangiocytes were delivered into the liver retrogradely through the extrahepatic biliary tree (14). In brief, a fine bore cannula was placed and secured in the gallbladder. To divert the infusion into the liver, the distal common bile duct was occluded with a clamp. The cells were infused through the cannula in the gallbladder in a total volume of 1μl/g of total body weight, at a maximum speed of 1μl/second.

MDA administration

Cholangiopathy was induced through intraperitoneal (IP) administration of 4,4′-methylene dianiline (MDA) on 3 occasions 7, 5, and 3 days prior to cell delivery at a concentration of 50 μg/g of total body weight. An additional dose of MDA was administered directly into the extrahepatic biliary tree prior to cell delivery as described above.

Blood sample collection

Blood was taken using a 23g needle directly from the inferior vena cava under terminal anesthesia at the time the animals were electively culled and transferred into 1.5ml Eppendorf tubes for further processing.

Blood sample processing

The blood samples were routinely processed by the University of Cambridge Core biochemical assay laboratory (CBAL). All of the sample analysis was performed on a Siemens Dimension EXL analyzer using reagents and assay protocols supplied by Siemens.

Tissue collection

Tissue for sectioning and staining was collected at the end of all animal experiments when the animals were culled, unless otherwise stated. The animals were culled due to due to animal welfare reasons (weight loss, jaundice and clinical deterioration) or electively 3 months after transplantation. Timepoints are indicated on the relevant Kaplan-Meier curves **(Fig. 3B; Fig. S13A).**

Cryosectioning

Excised tissue was fixed in 4% PFA, immersed in sucrose solution overnight, mounted in optimal cutting temperature (OCT) compound and stored at -80°C until sectioning. Sections

were cut to a thickness of 6-10µm using a cryostat microtome and mounted on microscopy slides for further analysis.

Haematoxylin and Eosin (H&E) Staining

H&E staining was performed by the histology service of Addenbrooke's hospital or using Sigma-Aldrich reagents according to the manufacturer's instructions. Briefly, tissue sections were hydrated, treated with Meyer's Haematoxylin solution for 5 minutes (Sigma-Aldrich), washed with warm tap water for 15 minutes, placed in distilled water for 30-60 seconds and treated with eosin solution (Sigma-Aldrich) for 30-60 seconds. The sections were subsequently dehydrated and mounted using the Eukitt® quick-hardening mounting medium (Sigma-Aldrich).

Histology

Histology sections were reviewed by an independent histopathologist with a special interest in hepatobiliary histology (SD).

Quantification of transplanted cells in mouse liver

For each animal 3 random sections were analyzed, with different lobes being assessed. A total of 49,846 cells were analyzed, approximately 10,000 cells per animal.

MR imaging

Magnetic resonance cholangio-pancreatography was performed after sacrifice of the animals. MRCP was performed at 9.4T using a Bruker BioSpec 94/20 system (Bruker, Ettlingen, Germany). For higher signal to noise ratio to give improved visualisation of the biliary ducts a two-dimensional sequence was used with slightly varied parameters (24 spaced echoes at 11ms intervals to give an effective echo time of 110ms; repetition time 5741ms; matrix size of 256×256; field of view of 4.33×5.35cm2 yielding a planar resolution of 170×200µm2). Slices were acquired coronally through the liver and gall bladder with a thickness of 0.6mm. For this acquisition, a volume coil was used to reduce the impact of radiofrequency inhomogeneity.

To examine the biliary tree, images were prepared by maximum intensity projections. Structural imaging to rule out neoplastic growths was performed using a T1-weighted 3D FLASH (fast low-angle shot) sequence with a flip angle of 25°, repetition time of 14ms and an echo time of 7ms. The matrix was 512×256×256 with a field of view of 5.12×2.56×2.56cm3 for a final isotropic resolution of 100 µm.

Volume rendered images of the biliary tree were generated from source data using Osirix software. The region of interest was segmented from the remaining data manually.

The MRCP images were reviewed by 2 independent radiologists with a special interest in hepatobiliary radiology (EMG, SU).

Ex vivo normothermic perfusion of donor livers

The *metra* (OrganOx, Oxford, UK) normothermic liver perfusion device was used for ex vivo perfusion of human livers as previously described (15, 30). The machine, which is clinically used for preservation of livers for transplantation (15) enables prolonged automated organ preservation by perfusing it with ABO-blood group-compatible normothermic oxygenated blood. The perfusion device incorporates online blood gas measurement, as well as software-controlled algorithms to maintain pH, PO2 and PCO2 (within physiological limits), temperature and mean arterial pressure within physiological normal limits. In brief, the hepatic artery, portal vein, inferior vena cava and bile duct were cannulated, connected to the device and perfusion commenced.

Bile duct cannulation

Cannulation of the bile duct was achieved by inserting two 4 Fr sheaths into the common bile duct under fluoroscopy guidance, followed by cannulation of the left and right hepatic ducts and subsequently segment 3 and segment 5 ducts respectively, using two 2.7 Fr microcatheters via the sheaths. Peripheral placement of the microcatheters was confirmed by cholangiogram with small amount of ionic contrast medium. Cells were injected into segment 3 and carrier was injected into segment 5.

Cell delivery

RFP-expressing organoids were mechanically dissociated to a mixture of small clumps and single cells and approximately 10x106 RFP-expressing cells were administered in a peripheral duct of segment 3 with a distribution area of ~2cm^3, which was cannulated under fluoroscopic guidance to maximize cell delivery (see Bile duct cannulation section) (**Fig. S15B**). Carrier medium was delivered in a peripheral branch of segment 5 using the same technique and the organ was maintained on NMP for up to 100 hours.

Quantification of transplanted cells in human livers

3 human livers injected with RFP-labelled gallbladder organoids were analysed. Sections were obtained from the area of the distribution of the cells (~2cm^3). 5 sections per liver and a total of 4,463 cells were analysed.

Bile aspiration

Bile duct cannulation was performed as described in the relevant section. Following cannulation, 2 microfluidic catheters (CMA Microdialysis Catheter, Harvard Biosience Inc, USA) were placed into the respective segmental ducts using a guide wire exchange technique. The inner and outer shaft of the catheter and the inlet and outlet tubing are made of polyurethane and the membrane composed of polyarylethersulphone with a membrane pore size of 100kDa and outer diameter of 0.4mm. The inlet tubing for each catheter was connected to a portable battery driven CMA 107 Microdialysis Pump (Harvard Biosience Inc, USA) and the pump was set to aspirate at a rate of 1µl/min.

Bile volume and pH measurements

Measurements were performed in n=3 different livers. A minimum of 2 repeat measurements were performed for each liver increasing to 3 where possible, as previously described (27). Bile volume was normalised over the volume of the bile ducts producing it, which corresponds to the volume of distribution of the cells or the carrier in the control arm. This was calculated using the volume of the contrast medium required to delineate these ducts on cholangiogram. Please note all catheters were primed prior to volume measurements.

Ultrasound imaging

The liver was imaged ex-vivo in a normothermic perfusion device using a Hitachi Aloka Arrieta V70 and a 10Mhz hand-held probe. Images were obtained in axial and sagittal planes and assessment of the portal vein, hepatic veins and their major branches was carried out. The intrahepatic bile ducts were also assessed, with particular attention to segment 3 where the organoids had been instilled, and a control area in segment 5 receiving carrier.

Statistical analysis

All statistical analyses were performed using GraphPad Prism 6. For small sample sizes where descriptive statistics are not appropriate, individual data points were plotted. For

comparison between 2 mean values a 2-sided Student's t-test was used to calculate statistical significance. The normal distribution of our values was confirmed using the D'Agostino & Pearson omnibus normality test where appropriate. Variance between samples was tested using the Brown-Forsythe test. For comparing multiple groups to a reference group one-way ANOVA followed by Dunnett's test was used between groups with equal variance, while the Kruskal-Wallis test followed by Dunn's test was applied for groups with unequal variance. Survival was compared using log-rank (Mantel-Cox) tests. Where the number of replicates (n) is given this refers to organoid lines or number of different animals unless otherwise stated.

For animal experiments, group sizes were estimated based on previous study variance. Final animal group sizes were chosen to allow elective culling at different time point while maintaining $n > 4$ animals surviving past 30 days to ensure reproducibility. No statistical methods were used to calculate sample size. No formal randomization method was used to assign animals to study groups. However, littermate animals from a cage were randomly assigned to experimental or control groups by a technician not involved in the study. No animals were excluded from the analysis. Blinding was used for radiology imaging.

Supplementary Figure 1

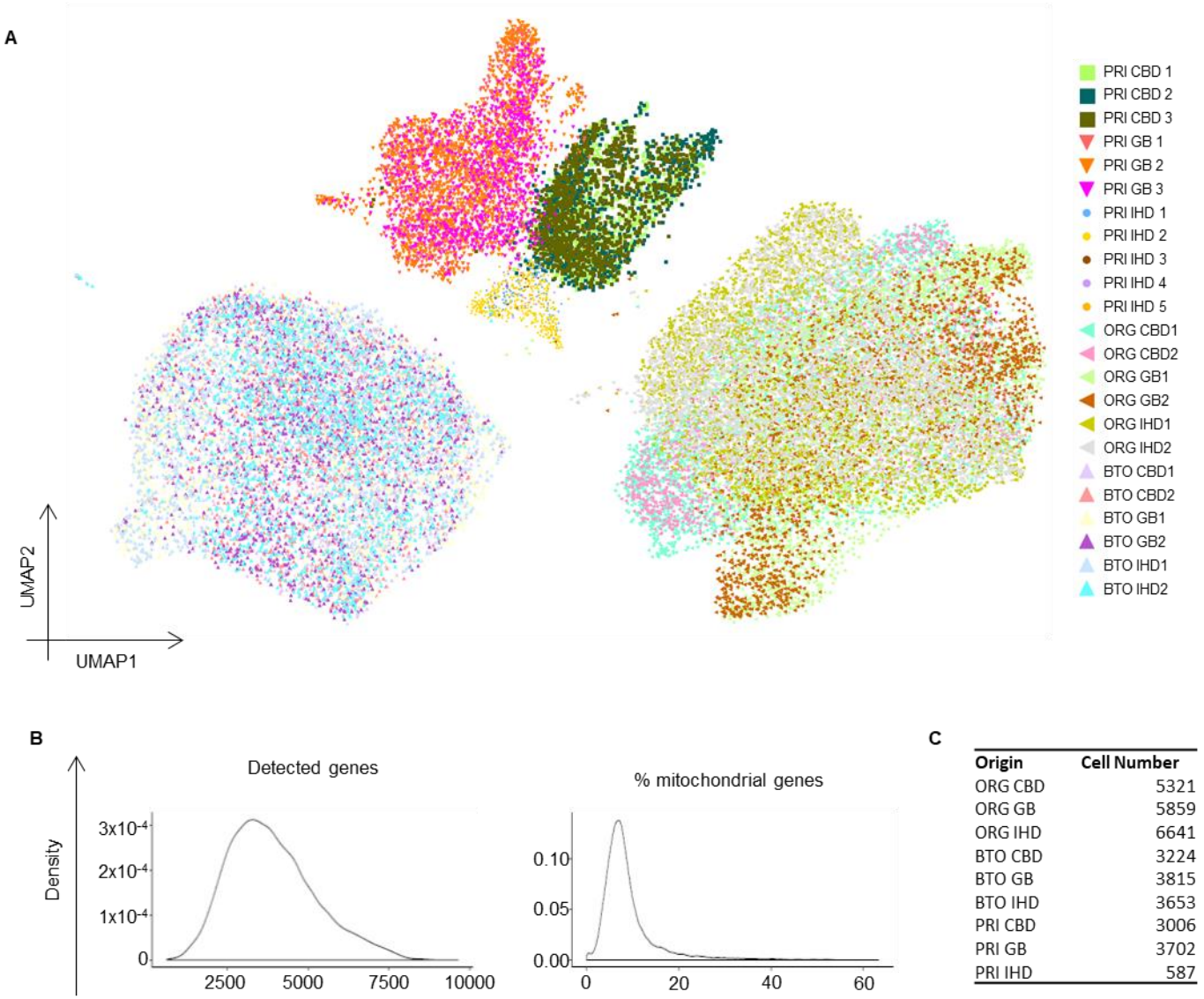

C

Origin	Cell Number
ORG CBD	5321
ORG GB	5859
ORG IHD	6641
BTO CBD	3224
BTO GB	3815
BTO IHD	3653
PRI CBD	3006
PRI GB	3702
PRI IHD	587

Fig. S1.

Characteristics and quality control of single cell RNA sequencing samples. (A) UMAP plot of all sequenced samples and 1 publicly available intrahepatic cholangiocyte dataset (PRI IHD 5; from MacParland SA et al, 2018, cluster 17). Each patient and cell line are distinguished by a unique color and marker combination. **(B)** Number of genes and percentage of mitochondrial genes detected per cell. **(C)** Number of cells isolated from each region PRI, Primary; IHD, IntraHepatic Ducts; CBD, Common Bile Duct; GB, Gallbladder; ORG, Organoids; BTO, Bile-treated organoids.

Supplementary Figure 2

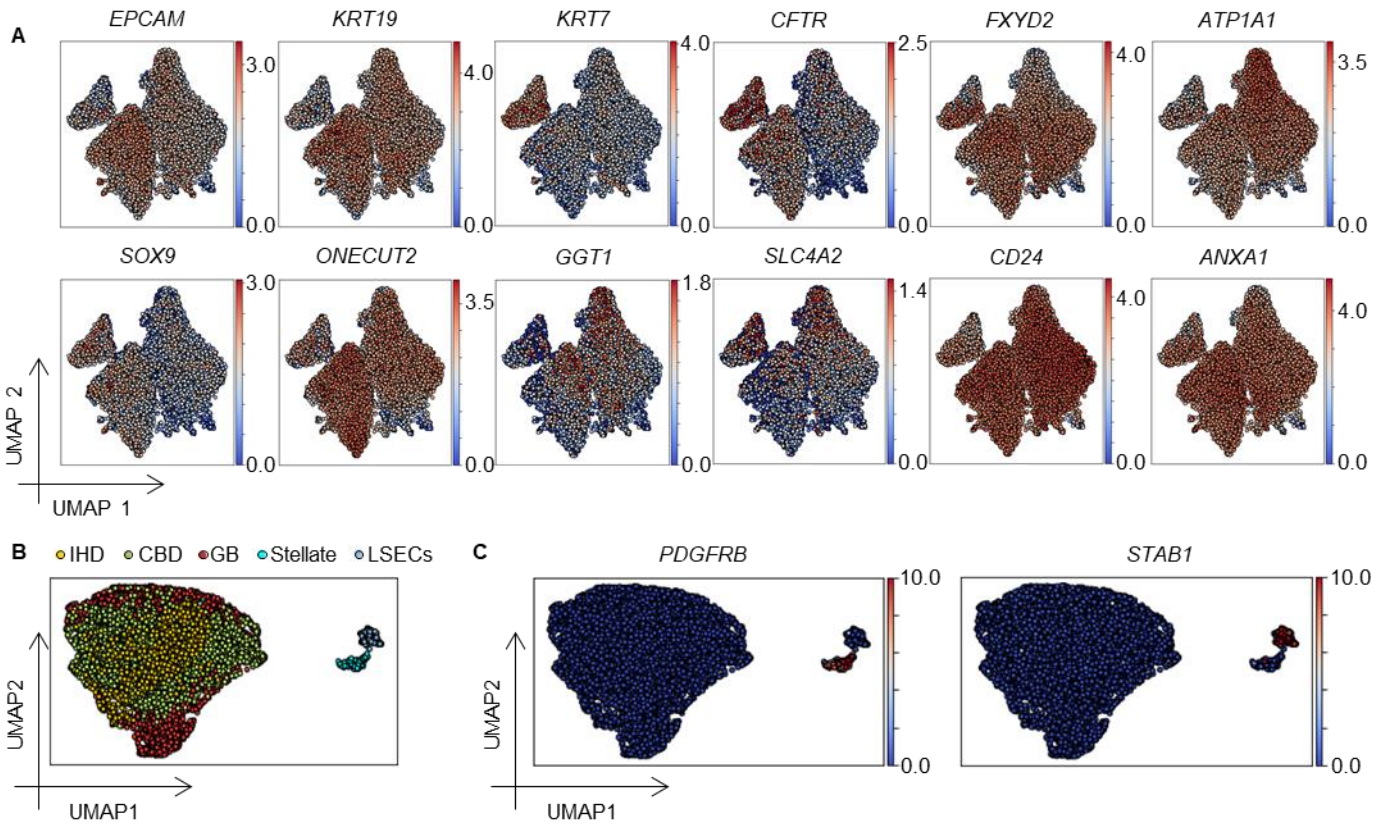

PAGA connectivity values

	LSECs	IHD	CBD	GB	Stellate
LSECs	N/A	0.25638	0.04901	0.08751	0.96648
IHD	0.25638	N/A	16.1408	13.0585	0
CBD	0.04901	16.1408	N/A	30.0574	0.16407
GB	0.08751	13.0585	30.0574	N/A	0.01627
Stellate	0.96648	0	0.16407	0.01627	N/A

Fig. S2.

Single cell RNA sequencing characterization of primary cholangiocytes. (A) UMAP plots demonstrating the expression of key cholangiocyte markers by the isolated cells, confirming their biliary identity. **(B)** UMAP plot of primary cholangiocytes compared to stellate and liver sinusoidal endothelial cells (LSECs) illustrating overlap between different region cholangiocytes when compared to a different cell type, which reflects a shared core biliary signature. **(C)** UMAP plots illustrating the expression of LSEC and stellate cell markers, confirming the cells' identity. **(D-E)** PAGA connectivity plot **(D)** and corresponding connectivity values **(E)** demonstrating a higher degree of transcriptional similarity between cholangiocytes from different regions compared to different cell types, confirming the shared core transcriptional signature of the cells. IHD, IntraHepatic Ducts; CBD, Common Bile Duct; GB, Gallbladder.

Supplementary Figure 3

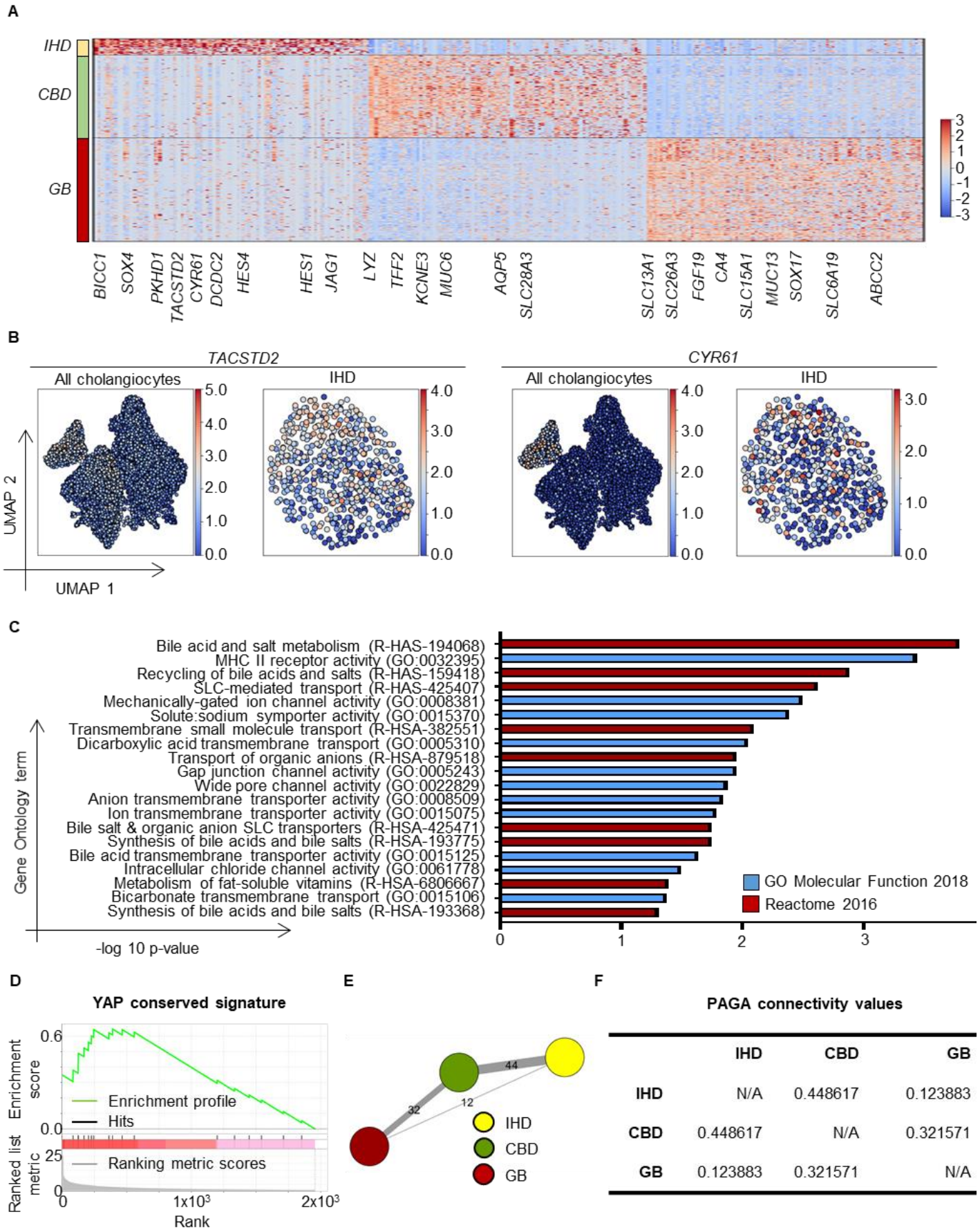

	IHD	CBD	GB
IHD	N/A	0.448617	0.123883
CBD	0.448617	N/A	0.321571
GB	0.123883	0.321571	N/A

Fig. S3.
Characterization of the transcriptional signature of cholangiocytes from different regions of the biliary tree. (A) Heatmap of top 100 Differentially Expressed Genes (DEGs) in cholangiocytes isolated from distinct regions of the biliary tree revealing transcriptional diversity in the primary biliary epithelium. IHD, IntraHepatic Ducts; CBD, Common Bile Duct; GB, Gallbladder (**Data S1**). **(B)** UMAP plots confirming the expression of previously described markers in IHDs. **(C)** Gene Ontology (GO) analysis on DEGs between biliary tree regions using EnrichR illustrating enrichment of cholangiocyte-to-niche interaction markers, such as bile processing and modifying genes. **(D)** Gene Set Enrichment Analyses on DEGs between biliary tree regions identifying differences in the expression of YAP target genes, $P<0.001$. **(E-F)** PAGA connectivity plot **(E)** and corresponding connectivity values **(F)** demonstrating a higher degree of transcriptional similarity between adjacent regions of the biliary tree. Connectivity values illustrated in **(E)** are multiplied by 100.

Supplementary Figure 4

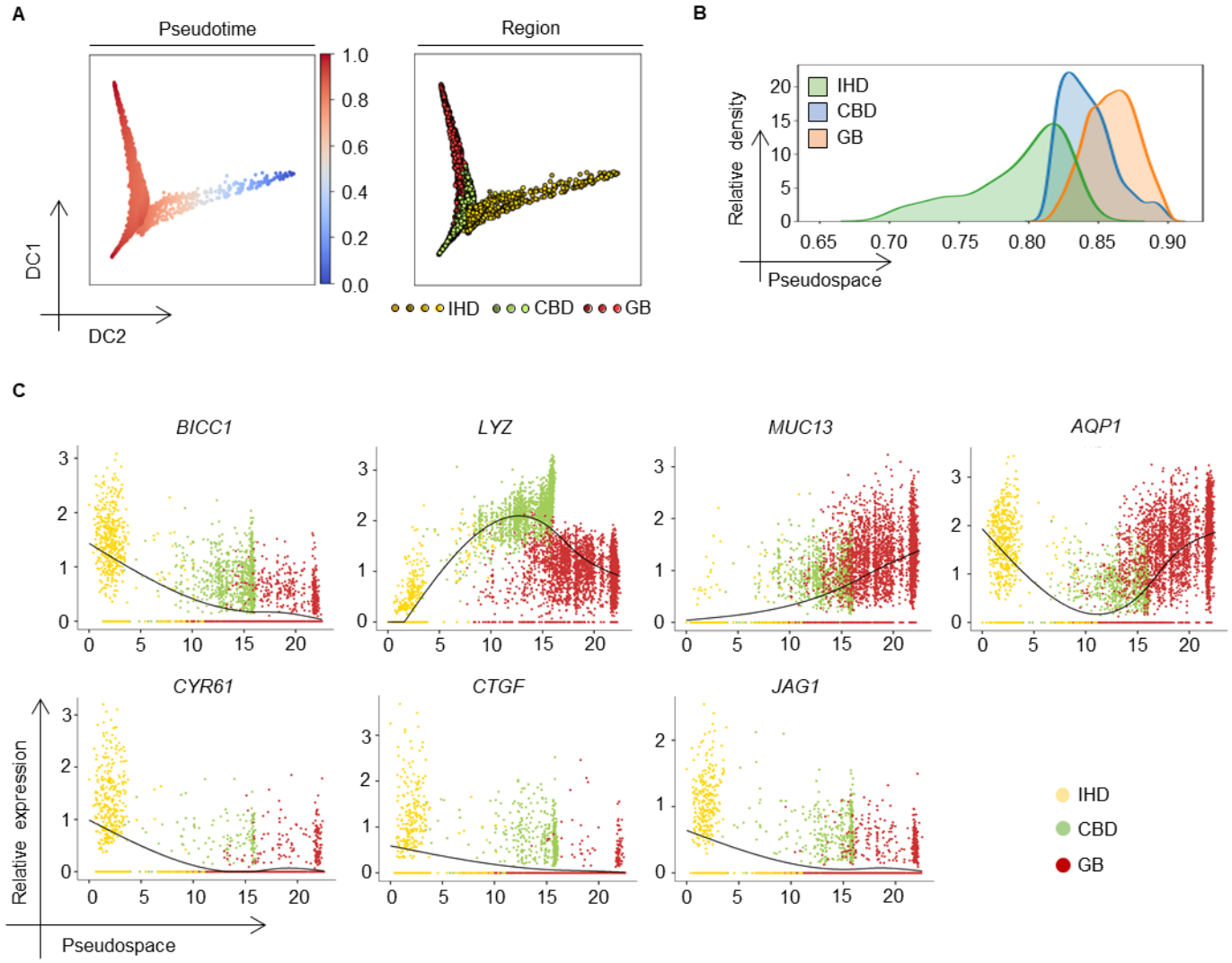

1

Fig. S4.

Pseudotime analysis of primary cholangiocytes. (A) Cell trajectory in pseudotime using Monocle; **(B)** Density plot of pseudo-time coordinates and **(C)** Gene expression in pseudotime of representative region markers indicating a gradual transition in transcriptional profile between cholangiocyte populations from adjacent regions. IHD: Intrahepatic Ducts, CBD: Common Bile Duct, GB: Gallbladder

Supplementary Figure 5

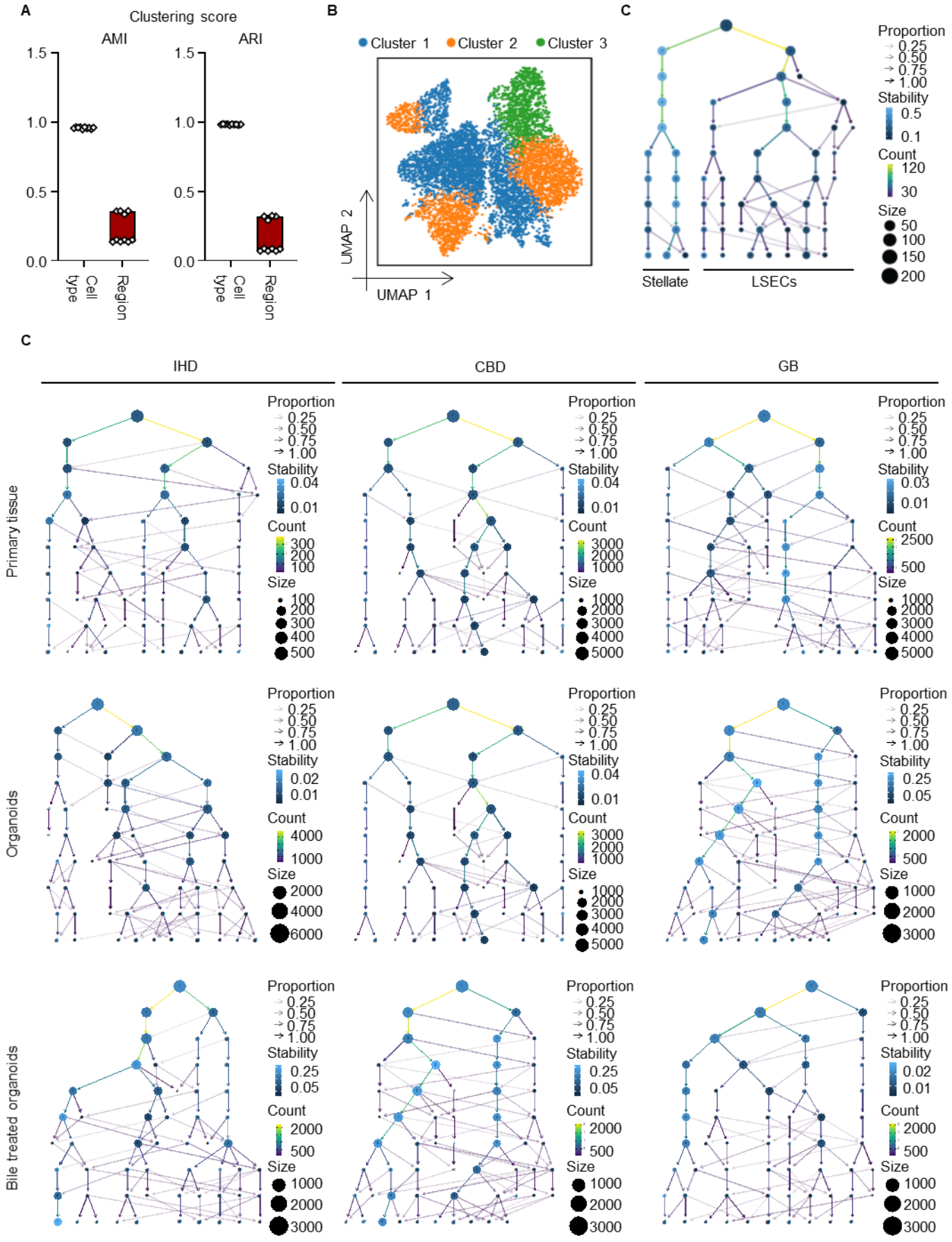

Fig. S5.

Characterization of cluster stability. (A) Adjusted Rand Index (ARI) and the Adjusted Mutual Information (AMI) confirming that primary cholangiocytes, organoids, and bile-treated organoids constitute distinct populations by illustrating a high correspondence between Louvain clusters and cell type (primary, organoids, bile-treated organoids) annotations (average value > 0.95 for both measures) vs. poor correspondence between Louvain clusters and region (intrahepatic ducts, common bile duct, gallbladder) annotations (average value<0.3 for both measures). **(B)** UMAP plot of Louvain clusters demonstrating poor matching between regions and clusters. The plot corresponds to the UMAP plot in **Fig. 1B** illustrating different regions. **(C-D)** Clustering trees derived from SC3 clusters by varying the pre-defined number of clusters k from 1 to 10 (see Methods) for a positive control comprising of stellate cells and LSECs **(C)** vs. cholangiocytes from different regions and corresponding cholangiocyte organoids **(D)**. Cluster stability across different clustering resolutions confirms the presence of different populations (stellate vs. LSECs) in the positive control **(C)**; while the absence of well-defined cholangiocyte subpopulations in each anatomical region or between organoids from different regions is demonstrated by the lack of stable clusters in **(D)**.

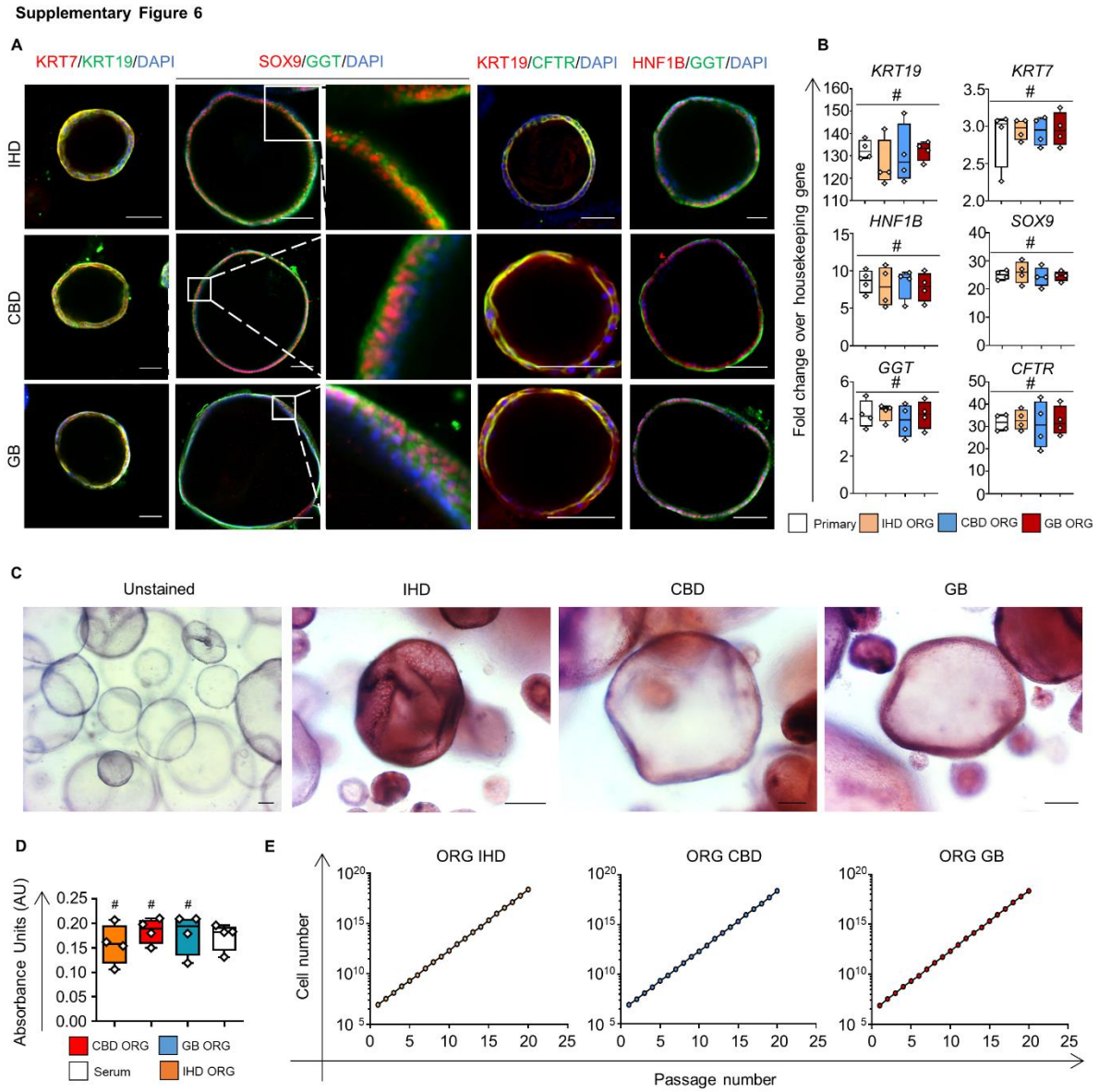

Fig. S6.

Characterization of cholangiocyte organoids from different regions of the biliary tree. (A) Immunofluorescence and **(B)** QPCR analysis of cholangiocyte organoids derived from different regions of the biliary tree demonstrating uniform expression of key biliary markers. n=4 samples per group; center line, median; box, interquartile range (IQR); whiskers, range; housekeeping gene, HMBS; #P>0.05#; scale bars, 50µm. **(C-D)** Organoids from different regions demonstrate Alkaline Phosphatase (ALP) **(C)** and GGT (Gamma-glutamyltransferase) **(D)** function. Scale bars, 100µm. **(E)** Growth curves illustrating comparable expansion potential between organoids from different regions. #, P>0.05. IHD, IntraHepatic Ducts; CBD, Common Bile Duct; GB, Gallbladder; ORG, Organoids; Primary, Primary CBD cholangiocytes.

Supplementary Figure 7

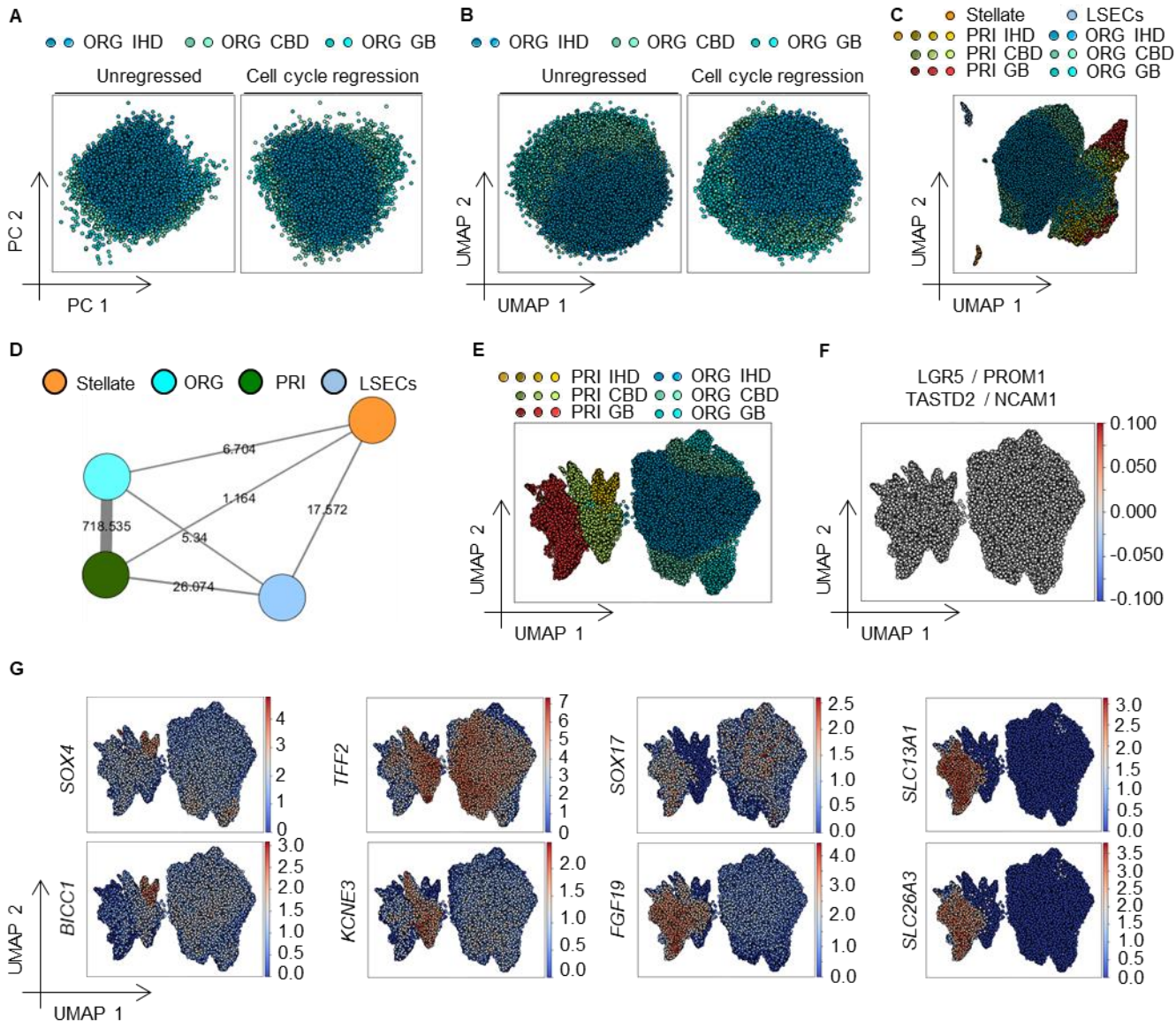

Fig. S7.

Single-cell RNA sequencing characterization of cholangiocyte organoids from different regions of the biliary tree. (A) PCA (unregressed, 24.8%; cell cycle regression, 21.8% of variance) and **(B)** UMAP representation demonstrating overlap in the transcriptional profile of different region organoids before and after cell cycle regression, confirming that cell cycle genes are not responsible for these similarities. **(C)** UMAP plot demonstrating that organoids and primary cholangiocytes irrespective of region occupy adjacent and overlapping spaces when compared to different cell types, illustrating a shared cholangiocyte transcriptional signature between biliary cells in vivo and in vitro. **(D)** PAGA connectivity plot demonstrating a higher degree of transcriptional similarity between cholangiocytes in vivo (PRI, Primary) and in vitro (ORG, organoids) compared to different cell types, confirming the shared core transcriptional signature of the cells. Respective connectivity values multiplied by 100 are illustrated on the plot. IHD, IntraHepatic Ducts; CBD, Common Bile Duct; GB, Gallbladder; LSECs, Liver Sinusoidal Endothelial Cells. **(E)** UMAP representation following regression of

cell cycle genes illustrating that the similarities between cholangiocyte organoids are preserved despite cell-cycle regression and therefore they are not attributable to a common 'proliferation' signature. **(F)** UMAP representation of cells co-expressing somatic stem cell markers (normalized expression>1), illustrating that similarities between organoids are not attributable to a common 'stem cell' signature. **(G)** UMAP representation of normalized gene expression values showing that organoids lose differences in the expression of region marks in culture.

Supplementary Figure 8

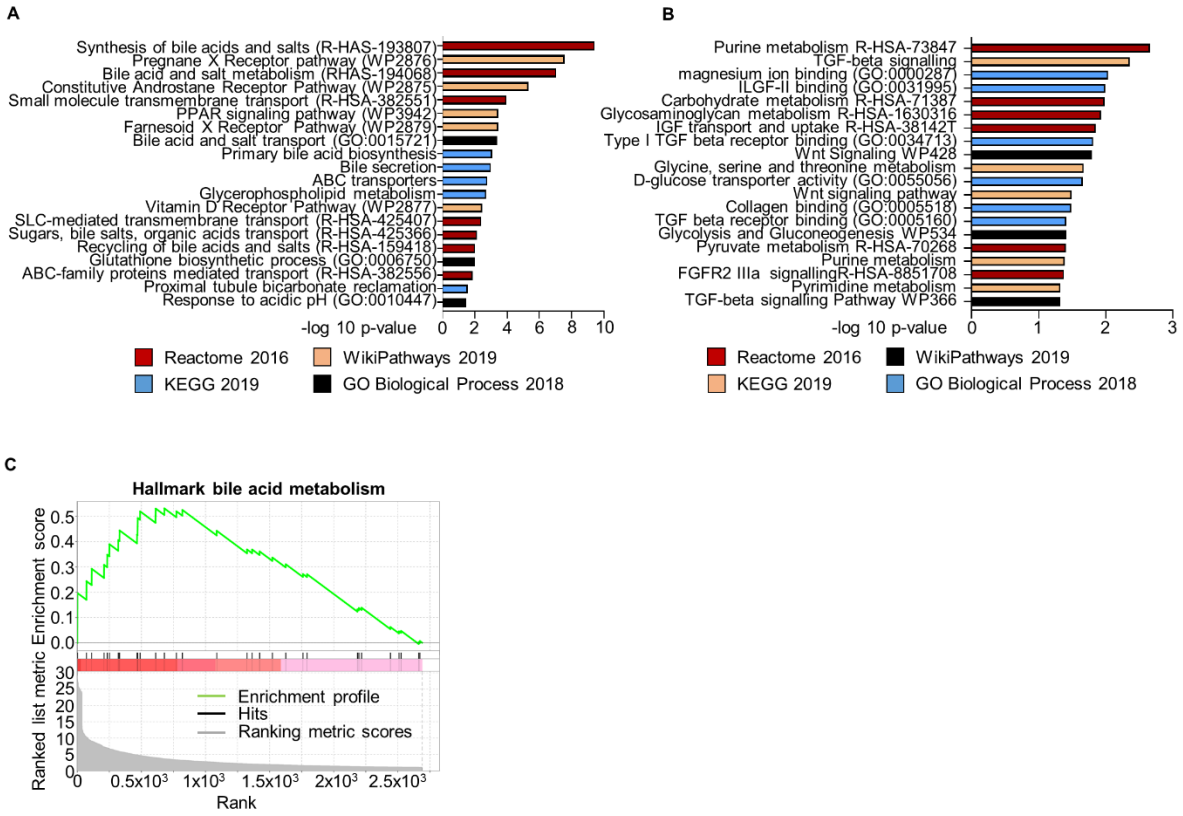

Fig. S8.

Gene ontology (GO) analyses on cholangiocyte organoids. (A-B) GO analysis on differentially expressed genes between primary cholangiocytes and organoids using EnrichR demonstrating that genes upregulated in primary tissue **(A)** are related to cholangiocyte-to-niche interaction, such as bile processing genes; while genes upregulated in organoids **(B)** reflect adaptation to cell culture conditions such as insulin, pyruvate and cytokine processing genes. **(C)** Gene Set Enrichment Analyses on DEGs between primary cells and organoids identifying differences in the expression of bile acid processing genes, *P*= 0.035. IHD, IntraHepatic Ducts; CBD, Common Bile Duct; GB, Gallbladder; ORG, Organoids.

Supplementary Figure 9

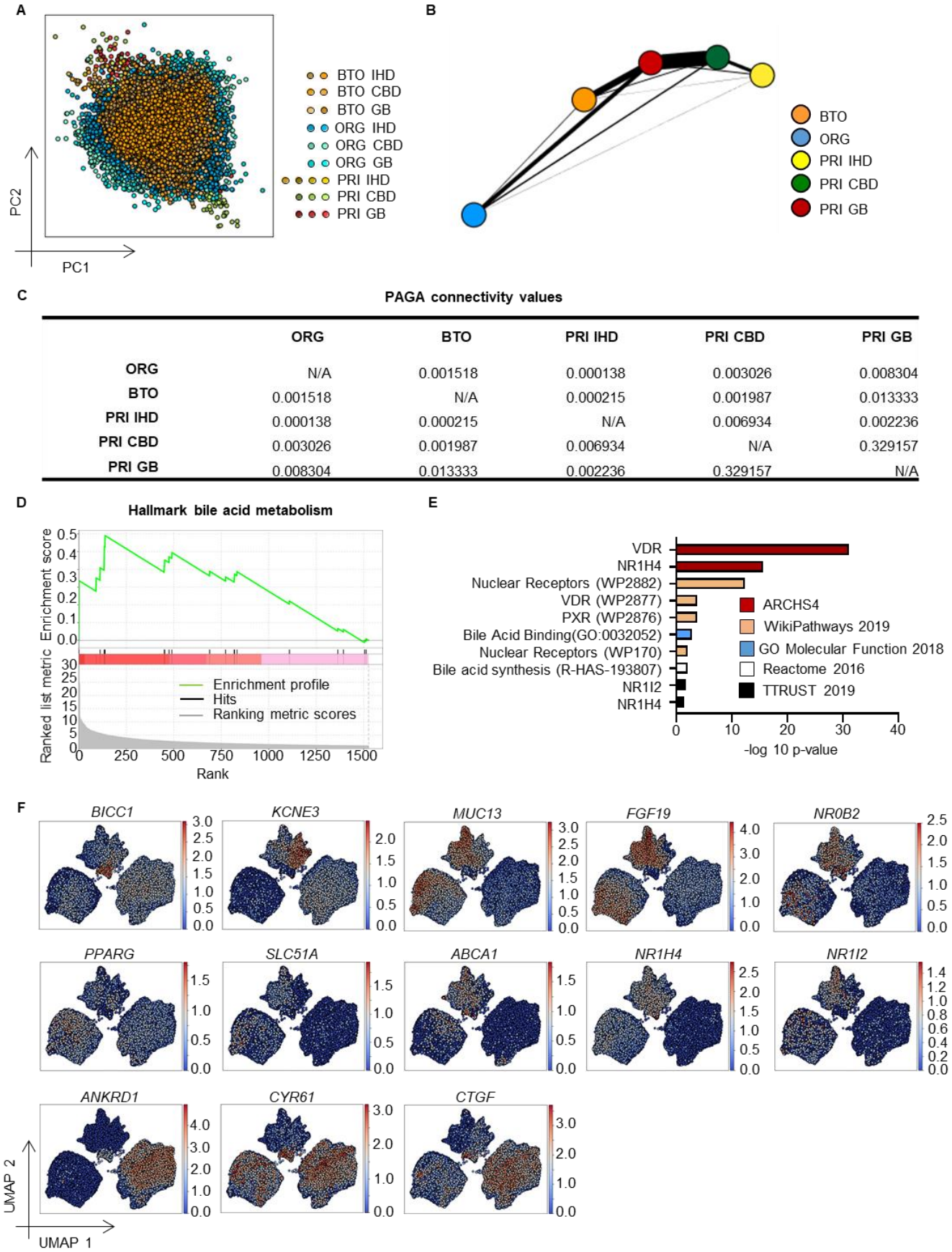

	ORG	BTO	PRI IHD	PRI CBD	PRI GB
ORG	N/A	0.001518	0.000138	0.003026	0.008304
BTO	0.001518	N/A	0.000215	0.001987	0.013333
PRI IHD	0.000138	0.000215	N/A	0.006934	0.002236
PRI CBD	0.003026	0.001987	0.006934	N/A	0.329157
PRI GB	0.008304	0.013333	0.002236	0.329157	N/A

1

Fig. S9.

Characterization of bile-treated organoids. (A) PCA analysis (16.8% of variance) showing overlap between organoids, primary cholangiocytes and bile-treated organoids irrespective of region suggesting a shared core transcriptional profile between all cells. **(B)** PAGA connectivity plot demonstrating that bile-treated organoids (BTO) shift their transcriptional profile towards primary gallbladder cholangiocytes. **(C)** Connectivity values corresponding to the PAGA connectivity plot in panel **(B)** IHD, IntraHepatic Ducts; CBD, Common Bile Duct; GB, Gallbladder; ORG, Organoids; BTO, Bile-treated organoids; PRI, Primary. **(D-E)** GSEA **(D)** and GO analysis using EnrichR **(E)** on differentially expressed genes in organoids before and after treatment with bile showing enrichment in bile processing genes and in particular bile acid nuclear receptors and their downstream targets. P=0.012. **(F)** UMAP representation of normalized gene expression values illustrating upregulation of gallbladder markers and bile acid downstream targets following treatment of organoids with gallbladder bile.

1

Supplementary Figure 10

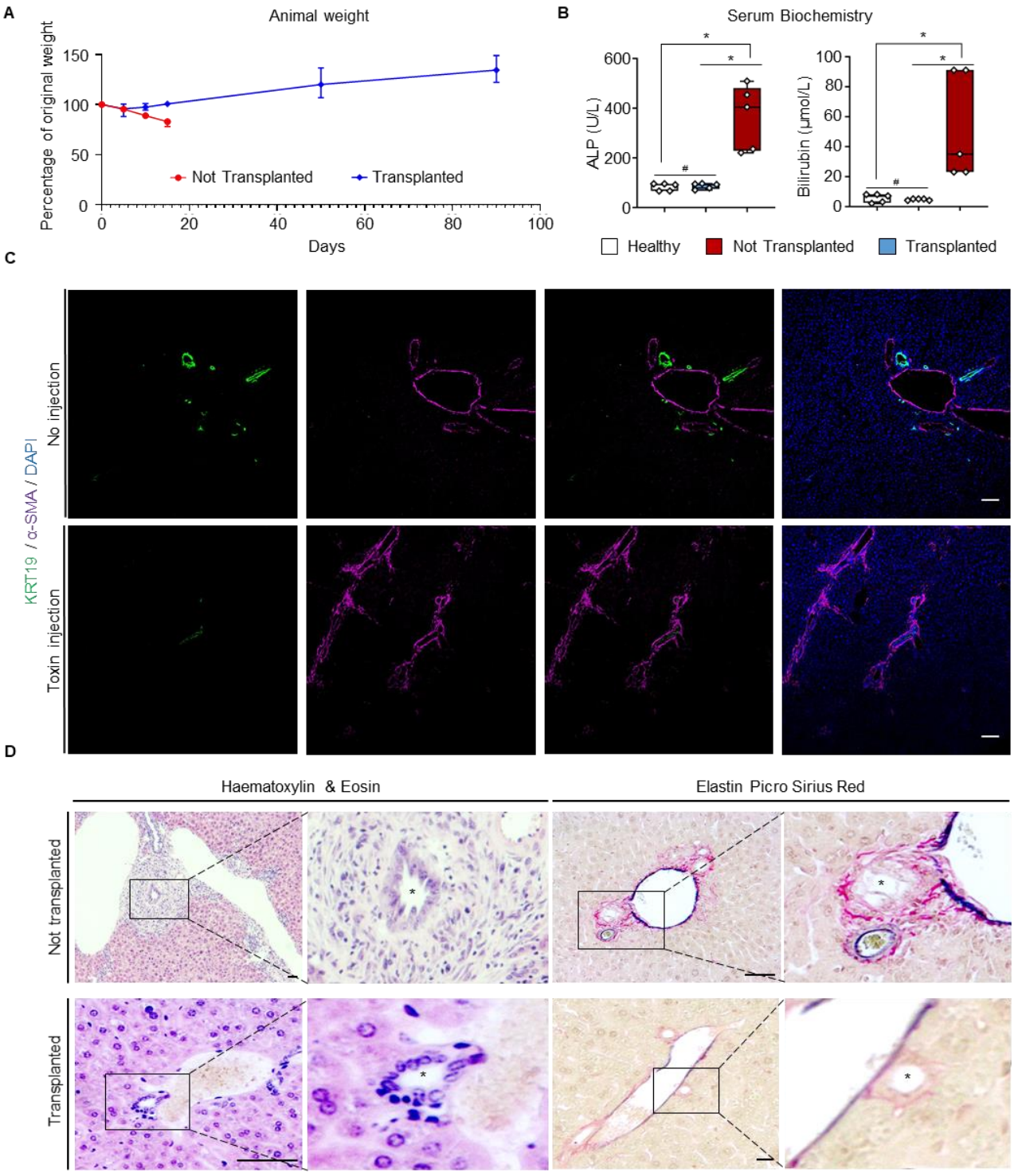

2

3

Fig. S10.

Gallbladder organoids rescue an acute cholangiopathy mouse model following transplantation. (A) Weight curve of animals treated with MDA (not transplanted) vs. animals injected with organoids following toxin treatment, demonstrating that injected animals recover and gain weight; n=5 animals in each arm. **(B)** Serum biochemistry demonstrating resolution of cholestasis following organoid injection; **P*<0.05, #*P*>0.05, Kruskal-Wallis test. **(C)** Immunofluorescence images of MDA treated animals not transplanted with cells (toxin injection) vs. untreated controls (no injection) illustrating biliary injury following MDA administration. The images are complementary to **Fig. 3D**. **(D)** Histology (Heamatoxylin & Eosin and Elastic Picro Sirius Red) illustrating resolution of cholangiopathy following organoid injection. Asterisks: Bile ducts.

Supplementary Figure 11

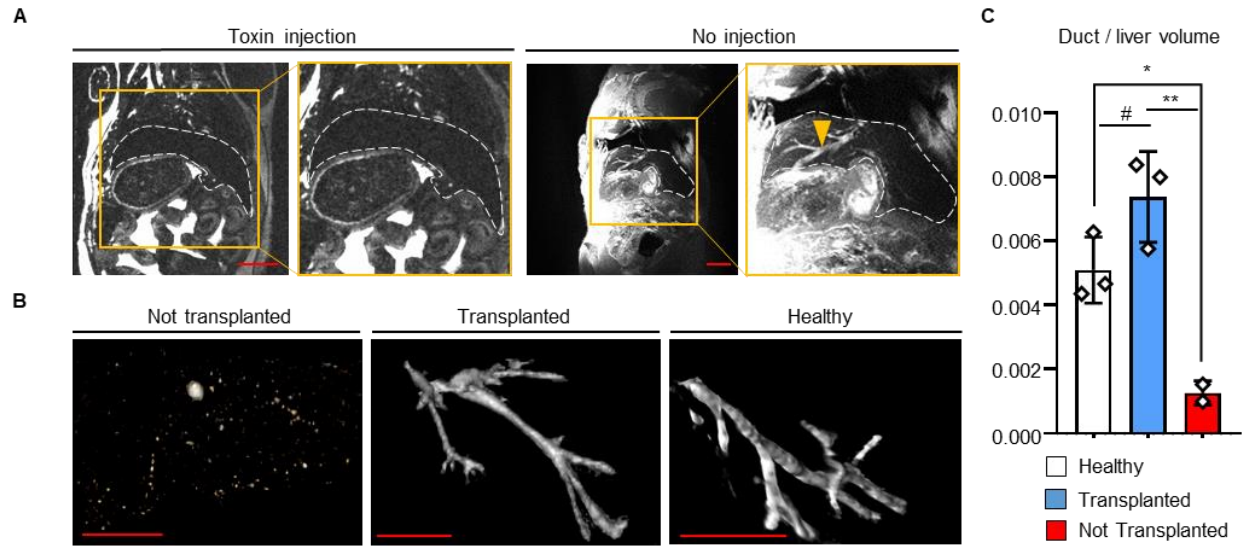

Fig. S11.
Gallbladder organoids regenerate the biliary tree of an acute cholangiopathy mouse model following transplantation. (A) Magnetic Resonance Cholangiopancreatography (MRCP) demonstrating biliary injury with loss of bile duct signal (white), immediately after toxin injection. The white dashed line outlines the liver margins. The image is complementary to **Fig. 3C.** Scale bars, 5mm. **(B)** 3D reconstruction of MRCP images demonstrating biliary injury with loss of bile duct signal in MDA-treated animals receiving carrier (not transplanted); vs. duct reconstruction in MDA-treated animals receiving organoid injections; vs. healthy animals. Scale bars, 5mm. **(C)** Quantification of bile duct signal on MRCP normalized over total liver volume in not transplanted vs. transplanted vs. healthy animals, demonstrating resolution of cholangiopathy following organoid injection; #, $P>0.05$; *, $P<0.05$; **, $P<0.01$; one-way ANOVA.

1 **Supplementary Figure 12**

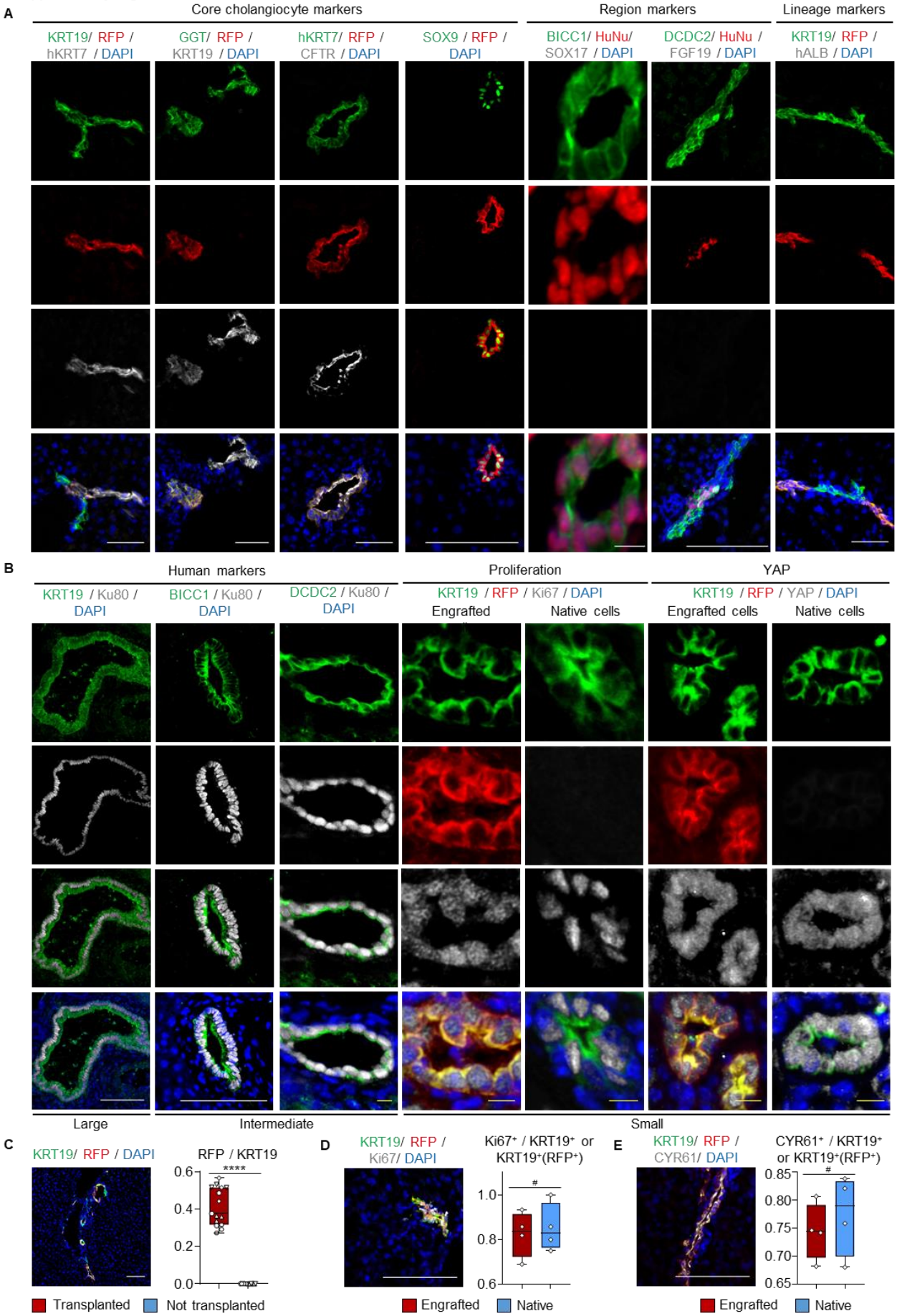

Fig. S12.
Gallbladder organoids regenerate the biliary epithelium of an acute cholangiopathy mouse model following transplantation. (A-B) Immunofluorescence analysis demonstrating engraftment, expression of key biliary markers, loss of gallbladder markers, expression of intrahepatic markers, absence of markers of other hepatic lineages **(A)**; and expression of human specific markers, proliferation markers and active YAP **(B)** in human Red Fluorescent Protein (RFP) expressing cells following transplantation in immunocompromised mice with cholangiopathy. Scale bars; **(A),** 50μm; **(B)**, 50μm (yellow), 100μm (white). The images are complementary to **Fig. 3**. **(C)** Quantification of human gallbladder-derived RFP-expressing cells in the bile ducts of transplanted vs. not transplanted animals; ** $P<0.01$; Mann-Whitney test. The data corresponds to 5 different animals and 3 random sections per animal. Each section is represented by a data point, while each animal is represented by a different symbol. **(D-E)** Quantification of the ratio of cells expressing proliferation markers (Ki67, **D**) and YAP downstream targets (CYR61, **E**) in ducts regenerated from engrafted human RFP-expressing cells vs. native mouse bile ducts in the same animals; # $P>0.05$; Mann-Whitney test.

Supplementary Figure 13

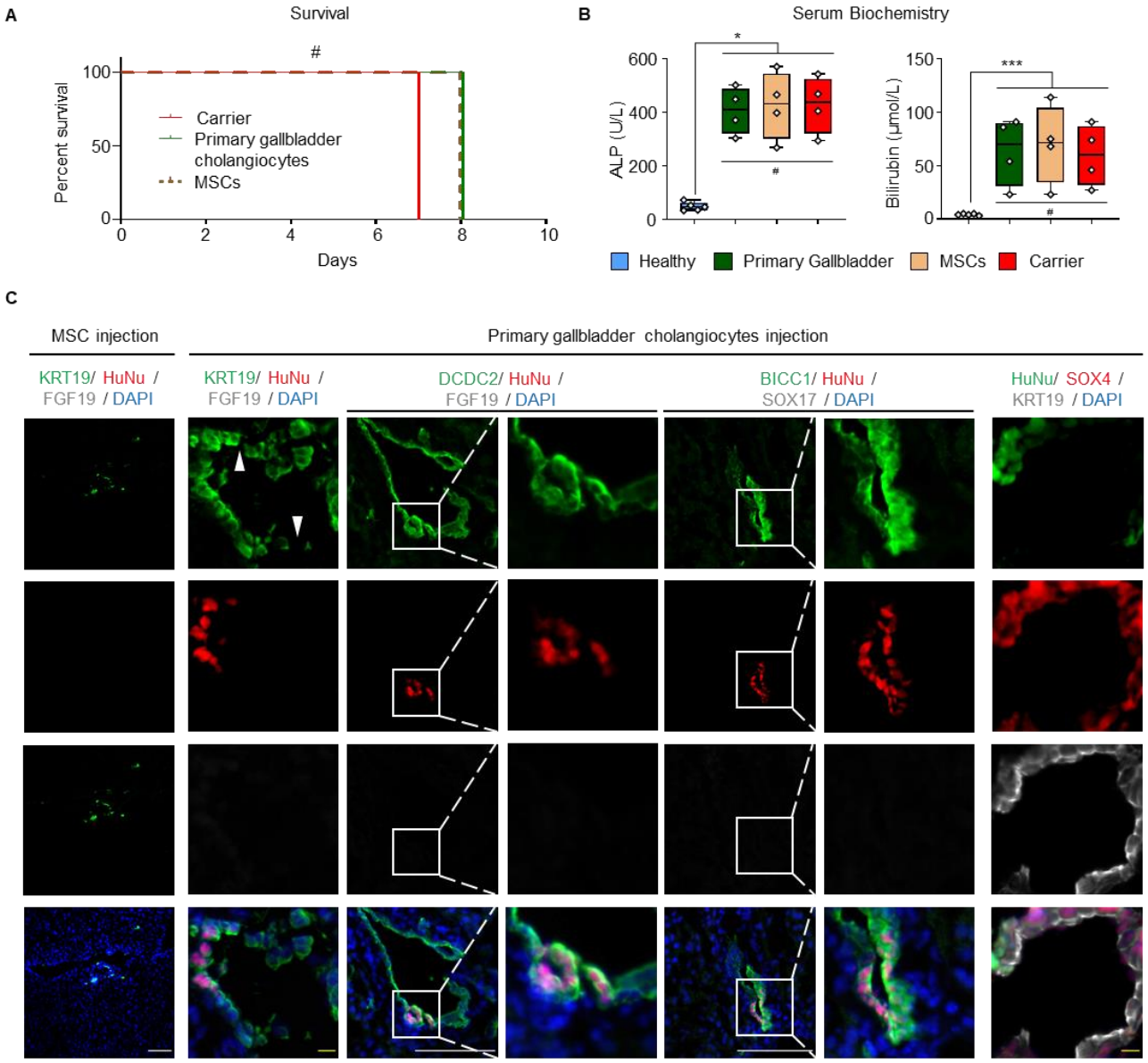

Fig. S13.

Primary human cholangiocytes and mesenchymal stem cells fail to rescue mice with acute cholangiopathy following transplantation. (A) Kaplan-Meier curve of mice with MDA-induced cholangiopathy receiving directly isolated human primary gallbladder cholangiocytes and human mesenchymal stem cells (MSCs) vs. carrier medium (carrier) demonstrating no statistically significant difference in survival between the three groups; $P>0.05$, log-rank test. **(B)** Serum biochemistry at the end of the experiment demonstrating persistent cholestasis in animals receiving primary gallbladder cholangiocytes, MSCs or carrier medium compared to healthy controls; $*P<0.05$, $***P<0.001$, #P>0.05, one-way ANOVA. **(C)** Staining for human markers following cell transplantation reveals lack of engraftment of MSCs; while primary gallbladder cholangiocytes exhibit low level engraftment, which was not adequate to repair the damaged bile duct epithelium (white arrowheads). Engrafted primary gallbladder cholangiocytes lose gallbladder markers and upregulate intrahepatic markers. Scale bars; white, 100µm; yellow, 10 µm.

Supplementary Figure 14

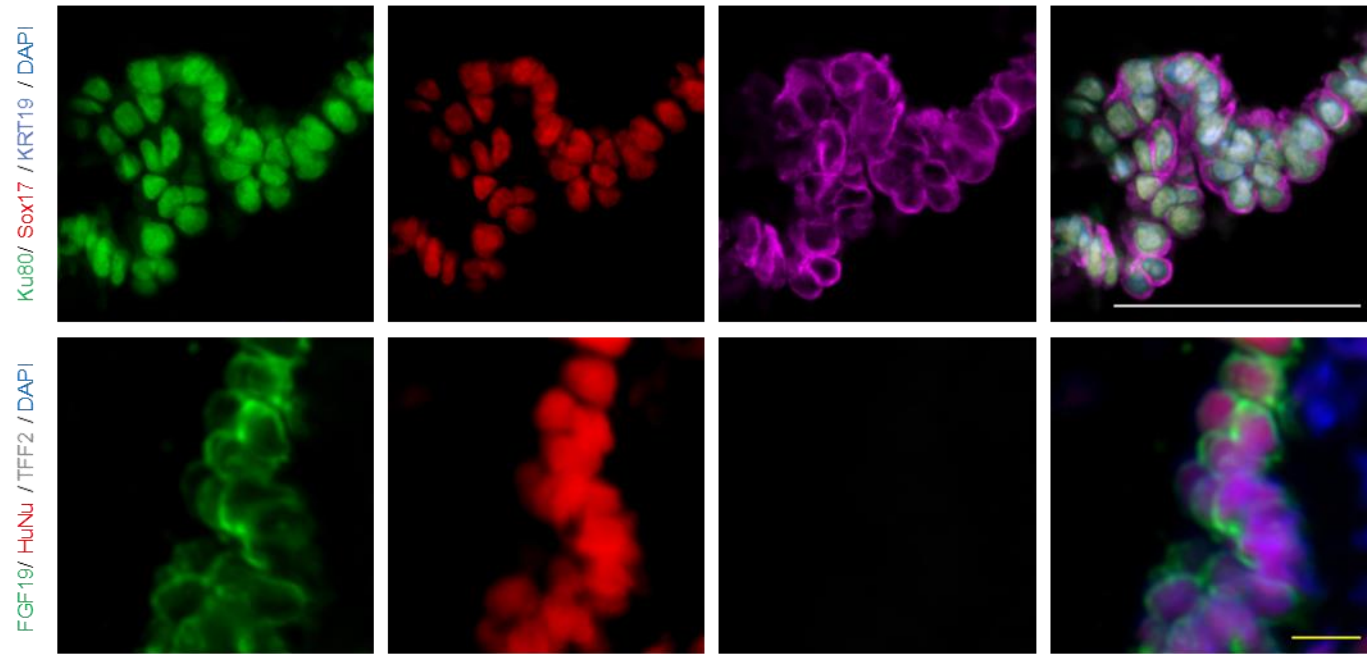

Fig. S14.
Transplantation of human common bile duct organoids in mouse gallbladder. Immunofluorescence analysis demonstrating expression of gallbladder markers and loss of common bile duct markers following transplantation of cholangiocyte organoids derived from human common bile duct in the gallbladder of immunocompromised mice. Scale bars; white, 100μm; yellow, 10μm.

Supplementary Figure 15

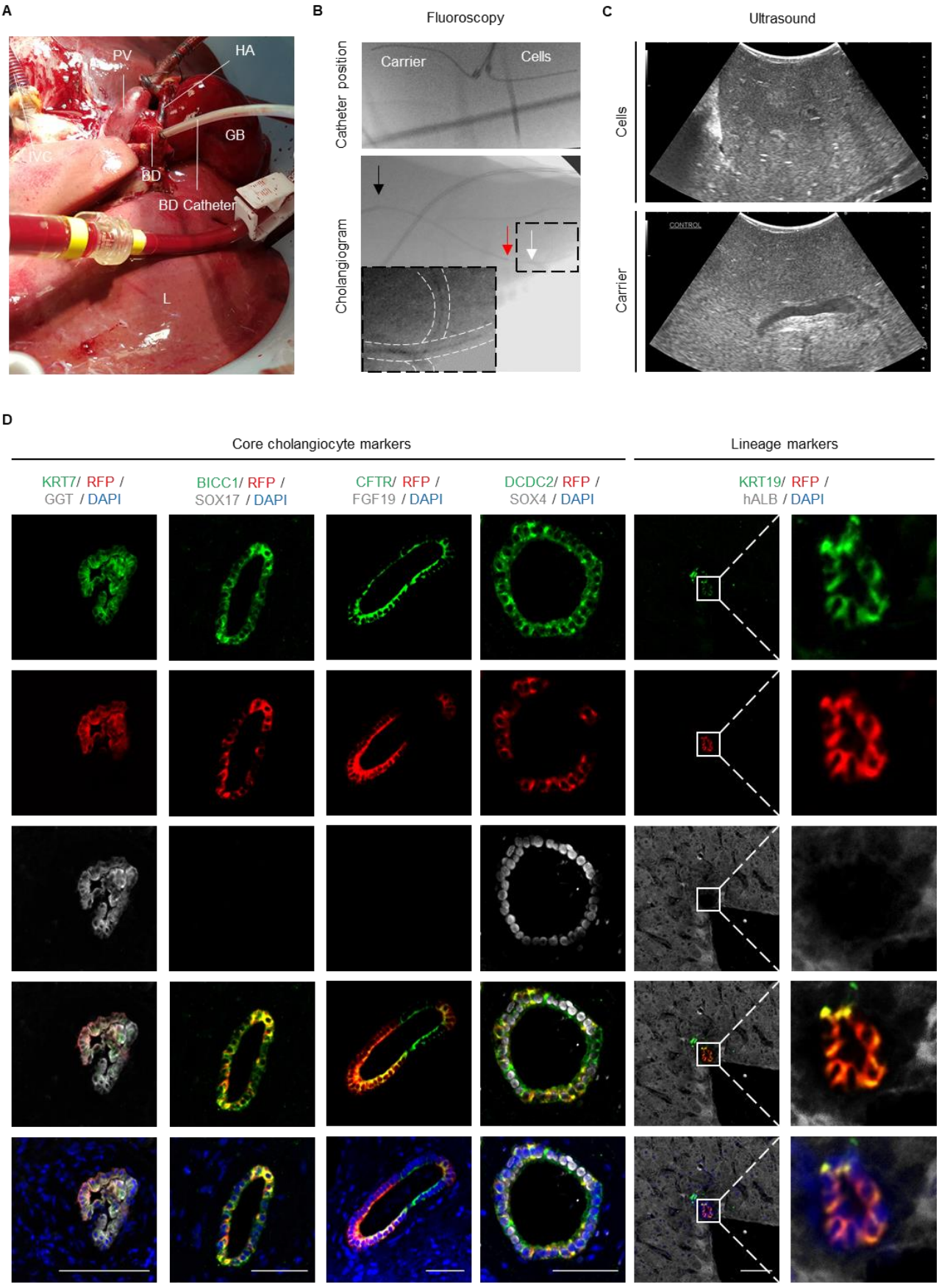

1

Fig. S15.

Administration of gallbladder organoids in human livers receiving Normothermic Perfusion (NMP). (A) Photograph of a human liver on NMP demonstrating anatomical landmarks, as well as the bile duct catheter used for administration of the Red Fluorescent Protein (RFP) expressing organoids. PV, portal vein; IVC, inferior vena cava; HA, hepatic artery; BD, Bile duct; GB, gallbladder; L, Liver. **(B)** Fluoroscopic images of peripheral duct cannulation. The position of the biliary catheters used for the injection of cells or carrier in the peripheral ducts of liver segments 3 and 5 respectively is shown in the top image. A cholangiogram of segment 3 following catheter placement, illustrating the peripheral position of the catheter and the area of distribution of injected the cells is shown in the bottom image. A magnified and contrast enhanced image is provided in the insert. Black arrow, sheath; red arrow, catheter tip; white arrow, cholangiogram. **(C)** Ultrasound imaging of the injected area of the liver revealing no duct dilation or any other abnormality at the end of the experiment. **(D)** Immunofluorescence analysis demonstrating engraftment, expression of key biliary markers, loss of gallbladder markers, expression of intrahepatic markers and loss of markers of other lineages in human Red Fluorescent Protein (RFP) expressing cells following transplantation in NMP human livers. Scale bars, 50μm. The images are complementary to **Fig. 4**.

Supplementary Figure 16

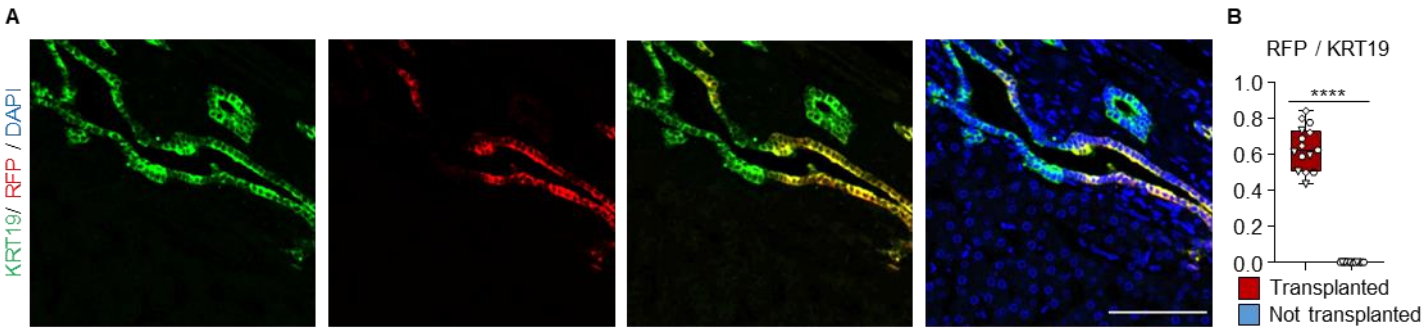

Fig. S16

Engraftment of gallbladder organoids in human livers receiving Normothermic Perfusion (NMP). (A) Immunofluorescence analysis demonstrating engraftment of human Red Fluorescent Protein (RFP) expressing cells following transplantation in NMP human livers. Scale bars, 100µm. The images are complementary to **Fig. 4, S15**. **(B)** Quantification of gallbladder-derived RFP-expressing cells in injected vs. not injected human bile ducts; **** $P<0.0001$, Mann-Whitney test. The data corresponds to 3 different livers and 5 random sections per liver. Each section is represented by a data point, while each organ is represented by a different symbol.

Table S1.

Table of the number of animals at risk corresponding to the Kaplan-Meier curve in **Fig. 3B**.

	Number of animals at risk	
Days	*Organoids*	*Carrier*
0	5	5
5	5	5
8	5	4
16	5	3
17	5	2
18	5	1
59	5	0
92	4	0

Table S2.

Table of antibodies used.

Antibody	Provider	Catalogue number	Dilution	Species
Anti-FGF19	Santa Cruz	sc-390621	1:100	Mouse
Anti-FGF19	Abcam	ab225942	1:100	Rabbit
Anti-TFF2	R&D systems	MAB4077	1:50	Mouse
Anti-DCDC2	Santa Cruz	sc-166051	1:100	Mouse
Anti-human albumin	R&D systems	MAB1455	1:50	Mouse
Anti-SOX4	Abcam	ab86809	1:50	Rabbit
Anti-SOX17	R&D systems	AF1924	1:100	Goat
Anti-RFP	Abcam	ab62341	1:100	Rabbit
Anti-RFP	Rockland	200-101-379	1:200	Goat
Anti-KRT19	DSHB	TROMA III	1:100	Rat
Anti-KRT19	Abcam	ab7754	1:100	Mouse
Anti-KRT19	Abcam	ab52625	1:100	Rabbit
Anti-KRT7	DAKO	GA61961-2	1:100	Mouse
Anti-KRT7	Abcam	ab68459	1:100	Rabbit
Anti-αSMA	DAKO	GA61161-2	1:100	Mouse
HNF1B (c-20)	SANTA CRUZ	sc-7411	1:100	Goat
GAMMA-GLUTAMYL TRANSPEPTIDASE (GGT)	Abcam	ab55138	1:100	Mouse
CYSTIC FIBROSIS TRANSMEMBRANE CONDUCTANCE REGULATOR (CFTR)	SANTA CRUZ	sc-10747	1:100	Rabbit
ALEXA FLUOR DONKEY ANTI-Rabbit 568	A10042	INVITROGEN	1:1000	Donkey
ALEXA FLUOR DONKEY ANTI-Rabbit 488	A21206	INVITROGEN	1:1000	Donkey
ALEXA FLUOR DONKEY ANTI-Rabbit 647	A31573	INVITROGEN	1:1000	Donkey
ALEXA FLUOR DONKEY ANTI-goat 568	A11057	INVITROGEN	1:1000	Donkey
ALEXA FLUOR DONKEY ANTI-goat 488	A11055	INVITROGEN	1:1000	Donkey
ALEXA FLUOR DONKEY ANTI-goat 647	A21447	INVITROGEN	1:1000	Donkey
ALEXA FLUOR DONKEY ANTI-mouse 568	A10037	INVITROGEN	1:1000	Donkey
ALEXA FLUOR DONKEY ANTI-mouse 488	A21202	INVITROGEN	1:1000	Donkey
ALEXA FLUOR DONKEY ANTI-mouse 647	A31571	INVITROGEN	1:1000	Donkey

Table S3

Table of QPCR primers used.

Gene		Primer sequence (5' à 3')
HNF1B	F	TCACAGATACCAGCAGCATCAGT
	R	GGGCATCACCAGGCTTGTA
PBGD	F	GGAGCCATGTCTGGTAACGG
	R	CCACGCGAATCACTCTCATCT
SOX9	F	CTCTGGAGACTTCTGAACGAGAG
	R	CCTTGAAGATGGCGTTGGGG
CK19	F	ACGACCATCCAGGACCTGCGG
	R	TCCCACTTGGCCCCTCAGCGTA
CK7	F	GATTGCTGGCCTTCGGGGT
	R	TCATCACAGAGATATTCACGGCTC
GGT	F	GTGAGAGCAGTTGGCTGTGC
	R	GTTGAACTCTGCTGTGGGGC
CFTR	F	AGTTGCAGATGAGGTTGGGC
	R	AAAGAGCTTCACCCTGTCGG
SOX4	F	AGCGACAAGATCCCTTTCATTC
	R	CGTTGCCGGACTTCACCTT
TFF2	F	CCCATAACAGGACGAACTGC
	R	GCACTGATCCGACTCTTGCT
SOX17	F	CGCACGGAATTTGAACAGTA
	R	GGATCAGGGACCTGTCACAC
FGF19	F	ATGCAGGGGCTGCTTCAGTA
	R	AGCCATCTGGGCGGATCT

Movie S1.

T1 weighted Magnetic Resonance Imaging (MRI) of a control mouse, receiving MDA followed by injection of carrier medium without organoids in the biliary tree.

Movie S2.

T2 weighted MRI/ Magnetic Resonance CholangioPancreatography (MRCP) of a control mouse receiving MDA followed by injection of carrier medium without organoids in the biliary tree demonstrating the presence of cholangiopathy. The MRCP sequence corresponds to the reconstructed MRCP image in Fig. 3C (not transplanted panel).

Movie S3.

T1 weighted Magnetic Resonance Imaging (MRI) of a mouse receiving MDA followed by injection of organoids in the biliary tree. The images were acquired 90 days after the injection of organoids demonstrating normal liver anatomy with no formation of tumors.

Movie S4.

T2 weighted MRI/ Magnetic Resonance CholangioPancreatography (MRCP) of a mouse receiving MDA followed by injection of organoids in the biliary tree demonstrating resolution of cholangiopathy. The MRCP sequence corresponds to the reconstructed MRCP image in **Fig. 3C** (transplanted panel).

Movie S5

MRI-based 3D reconstruction of the biliary tree of a control mouse receiving MDA followed by injection of carrier medium without organoids in the biliary tree demonstrating the presence of cholangiopathy with loss of bile duct signal. The bile ducts were reconstructed from T2 weighted MR images.

Movie S6

MRI-based 3D reconstruction of the biliary tree of a mouse receiving MDA followed by injection of organoids in the biliary tree demonstrating resolution of cholangiopathy. The bile ducts were reconstructed from T2 weighted MR images.

Movie S7

Z-stack of native and regenerated RFP-expressing bile ducts in the liver of an animal receiving MDA followed by injection of RFP-expressing human gallbladder organoids in the biliary tree. KRT19 is shown in green. RFP is shown in red. The movie is complementary to **movies S8** and **S9**.

Movie S8

3D reconstruction illustrating native and regenerated bile ducts in the liver of an animal receiving MDA followed by injection of RFP-expressing human gallbladder organoids in the biliary tree. Native ducts, KRT19 positive/ RFP negative; regenerated ducts, KRT19 positive/ RFP positive. The bile ducts were reconstructed from the RFP and KRT19 immunofluorescence images used to generate **movie S7**. KRT19 is shown in green, RFP is shown in red. The movie is complementary to **movies S7** and **S9**.

Movie S9

3D rendering illustrating native and regenerated bile ducts in the liver of an animal receiving MDA followed by injection of RFP-expressing human gallbladder organoids in the biliary tree. Native ducts, KRT19 positive/ RFP negative; regenerated ducts, KRT19 positive/ RFP positive. The bile ducts were reconstructed from the RFP and KRT19 immunofluorescence images used to generate **movie S7** and **S8**. KRT19 is shown in green, RFP is shown in red. The movie is complementary to **movies S7** and **S8**.

Data S1. (separate file)

Table of differentially expressed genes between different regions of the biliary tree. IHD, Intrahepatic ducts; CBD, Common Bile Duct; GB, Gallbladder. The table corresponds to genes with a log2 fold change > 1 and an adjusted *P* value < 0.001.

Data S2. (separate file)

Table of differentially expressed genes in pseudotime in primary cholangiocytes with an adjusted *P* value<0.001.

Data S3. (separate file)

Table of differentially expressed genes upregulated in organoids or organoids treated with bile versus primary cholangiocytes. ORG, organoids; ORGT, Bile treated organoids. The table corresponds to genes with a log2 fold change > 1 and an adjusted *P* value < 0.001.